Nonlinear Dyn (2024) 112:4085–4115
https://doi.org/10.1007/s11071-023-09268-y

ORIGINAL PAPER

Nonlinear vibration and superharmonic resonance analysis of wind power planetary gear system

Shuai Mo · Yiheng Liu · Xuan Huang · Wei Zhang

Received: 26 April 2023 / Accepted: 26 December 2023 / Published online: 29 January 2024

Abstract The nonlinear dynamic model of the NW (planetary gear structure with internal and external meshing and without planet carrier) planetary gear bearing was established in this study, taking into account factors such as random wind speed, time-varying support stiffness, bearing clearance, transmission error, tooth backlash, flexible ring gear, time-varying meshing stiffness, and tooth surface friction. The system's nonlinear behavior was described using phase trajectory plane, time–frequency analysis, time history, 3D frequency spectrum, FFT spectrum, phase diagram, and Poincaré map, as well as bifurcation diagram. Additionally, the superharmonic resonance characteristics of the system were analyzed using a multi-scale method, and the stability conditions for superharmonic resonance were determined through numerical analysis. Furthermore, the effects of meshing damping, displacement control parameters, and speed control parameters on the amplitude–frequency characteristics of the NW planetary gear-bearing system were examined. The conclusions indicate that the NW planetary gear-bearing system exhibits various nonlinear characteristics, and the system's stability can be improved by increasing damping and selecting appropriate time delay parameters.

Keywords Nonlinear dynamics · NW planetary gear · Time-varying support stiffness · Ring gear flexibility · Bifurcation and chaotic · Superharmonic resonance

1 Introduction

The old energy structure is gradually evolving as society and technology improve, and renewable green energy will eventually overtake fossil fuels as the primary energy source. The most popular renewable energy is wind energy, which is also one of the trends of new energy development in the future. [1, 2]. As an

---

Shuai Mo and Yiheng Liu contributed equally to this work, they are co-first authors of the article.

S. Mo (✉) · Y. Liu · X. Huang · W. Zhang (✉)
State Key Laboratory of Featured Metal Materials and Life-Cycle Safety for Composite Structures, Guangxi University, Nanning 530004, China
e-mail: moshuai2010@163.com

W. Zhang
e-mail: sandyzhang9@163.com

S. Mo · Y. Liu · X. Huang · W. Zhang
School of Mechanical Engineering, Guangxi University, Nanning 530004, China

S. Mo
State Key Lab of Digital Manufacturing Equipment and Technology, Huazhong University of Science and Technology, Wuhan 430074, China

S. Mo
National Key Laboratory of Science and Technology on Helicopter Transmission, Nanjing 210016, China

important component of wind turbines, gearboxes play an important role in wind power generation, because they can transmit power and change speed. Because of its wide transmission ratio range, traits of compact radial size, and high transmission efficiency, NW-type (planetary gear structure with internal and external meshing and without planet carrier) planetary transmission structure is gradually reused and employed in high-power wind turbine turbochargers. In order to determine the working conditions of NW wind turbines, the nonlinear dynamic analysis of the NW planetary gear structure is very necessary.

The nonlinear behavior and superharmonic resonance features of gear systems have been extensively studied by many academics for a variety of reasons. Many researchers have created nonlinear dynamic models and taken into account the impacts of pitch deviation, tooth backlash, and tooth center deviation. [3–6]. Wang and Zhu [7–9] researched the effects of meshing stiffness, tooth surface friction, tooth backlash, and bearing clearance, and established a geared turbofan engine gearbox's fixed-axis straight-tooth planetary gear-rotor-bearing system's nonlinear dynamic model. Many studies have considered the temperature rise caused by gear friction and established dynamic models, including nonlinear factors such as gear thermal deformation. [10–13]. Mo et al. [14–16] studied the evolution of nonlinear global behavior of non-orthogonal face gear-bearing system, described the development of the overall behavior of the system with excitation frequency, load change, and meshing damping, and studied the asymmetric meshing characteristics and load sharing characteristics of gears. Shuai et al. [17, 18] studied the nonlinear vibration characteristics of non-orthogonal face gear-bearing system and the load sharing characteristics of elastically supported herringbone planetary gear train and floating sun gear. Zhao et al. [19] Li et al. [20] Wei et al. [21] Xiang et al. [22] Qiu et al. [23] established a nonlinear model of planetary gear transmission system considering the factors such as segmented clearance, gravity, pitch, and inclination of the table.

Wind power accelerator is an important part of wind turbines, many scholars have undertaken extensive research on it. Zhao et al. [24] conducted a study on the impact of external excitation, mesh stiffness, and static transmission error on the torsional vibration of wind turbine transmission systems. Chen et al. [25] investigated the effects of random wind speed and random backlash on the vibration of wind turbine transmission systems. Guo et al. [26] employed the modified harmonic balance method with simultaneous excitation to study the dynamics of wind turbine planetary gear sets under the influence of gravity. Zhu et al. [27] developed a coupled dynamic model for wind turbine gearboxes with flexible pinions. Zhang et al. [28] considered the different meshing of the internal and external teeth of the planetary gear and the mixed effect of elastic hydrodynamic lubrication and boundary lubrication when analyzing the composite gear transmission system of wind turbines.

The multi-scale method was proposed by Sturrock, Cole, Nayfeh, et al. and then further developed later. Moradi and Salarieh [29] used a multi-scale method to study the forced vibration response of a single-degree-of-freedom gear system, including nonlinear factors such as gear clearances. Wang et al. [30] examined the parametric resonance and stability of cracked gear systems; he then used the multi-scale method to show how important parameters like damping ratio affected the stability of the system.

The current research on transmission systems mainly focuses on single-stage gear pairs with multi-factor coupling and planetary gear systems with single or few-factor couplings. However, there is a lack of studies on the nonlinear dynamics modeling of the entire transmission system under multi-factor coupling effects. This paper establishes a nonlinear dynamics model of a wind turbine transmission system considering multiple factors such as random wind speed, time-varying mesh stiffness, time-varying support stiffness, tooth backlash, gear flexibility, and tooth surface friction. It also takes into account the coupling effects of bearings in the planetary gear system, as well as the influence of bearing clearance. By incorporating multiple parameters into the coupled transmission system model described above, the resulting nonlinear dynamics model becomes more realistic and accurate, leading to higher precision.

The primary objective of this paper is to analyze the nonlinear dynamic response and superharmonic resonance properties of the NW planetary gear-rotor bearing system, considering factors such as random input load, time-varying meshing stiffness, flexible ring gear, tooth backlash, transmission error, bearing clearance, and friction. The structure of this paper is as follows: In Sect. 2, the dynamic model of the NW planetary gear-bearing system is created, including the input model considering random wind speed input, bearing force analysis with bearing clearance, calculation model of helical gear friction, and force analysis of the inner ring gear considering flexibility. Section 3 develops the vibration differential equation of the NW planetary gear-bearing system. Section 4 elaborates on the impact of excitation frequency on the NW planetary gear-bearing system, presenting time history, frequency diagram, phase diagram, Poincaré map, time–frequency, phase trajectory plane, and 3D frequency spectrum. Section 5 derives the stability condition of superharmonic resonance of the NW planetary gear-bearing system using the multi-scale method, and simulates the influence of meshing damping, displacement control parameters, and speed control parameters on superharmonic resonance using the numerical method. Finally, Sect. 6 draws the conclusion.

Through the above 6 sections, we can get that the NW planetary gear-bearing system exhibits various nonlinear characteristics. Meshing damping, velocity delay parameters, and displacement delay parameters have obvious influence on the amplitude of the system. The stability of the system can be improved by increasing the damping and selecting the appropriate time delay parameters.

2 NW planetary gear nonlinear model

2.1 NW wind power gear model

Figure 1 depicts the structure of the NW wind power accelerator transmission, which consists of a first-stage NW planetary gear and a first-stage parallel-axis herringbone gear. The power generated by natural wind driving the blade is input through the inner gear ring, and after passing through the gear structure, it is output by the herringbone gear. In this context, Tin and Tout represent the input torque and output torque, while r, p, s, and h denote the inner ring gear, planetary gear, sun gear, and herringbone gear, respectively.

2.2 Random wind speed

The natural wind drives the wind blades, forming the input torque of the NW wind power planetary gearbox, hence the pattern of natural wind speed change has a significant impact on the input torque. In this article, a two-parameter Weibull distribution with a shape parameter of 5.0 and a scale value of 11.5 is employed to simulate the speed of natural wind. Figure 2 shows the random wind speed within 400 s.

Weibull distribution model:

$$F(v) = 1 - e^{-\left(\frac{v}{c}\right)^k} \tag{1}$$

where K represents the shape parameter, which is used to explain how observations of wind speed vary, C represents the scale parameter which is connected to the mean wind speed, and v is wind speed.

For NW wind turbine, the variation of the input speed and input torque of the gearbox is depicted in Fig. 3. When the natural wind speed is between the cut-in wind speed and the rated wind speed, the variation of the input torque and the input speed with the wind speed is depicted in Eq. (2).

$$\begin{cases} T_{\mathrm{in}} = \dfrac{T_e}{v_e^2} v^2 \\ v_{\mathrm{in}} = \dfrac{v_{\mathrm{vate}}}{v_e} v \end{cases} \tag{2}$$

where T_e is the rated torque, v_e is the rated wind speed, and v_{vate} is the rated speed.

Depending on the characteristics of the NW wind turbines shown in Table 1, the input speed and torque versus time curves of the NW wind turbine gearbox are depicted in Fig. 4.

2.3 Time-varying mesh stiffness

The meshing of helical gear and herringbone gear begin at one end of the tooth and gradually spread to the entire tooth surface, and the meshing stiffness without mutation point. Figure 5 shows the meshing stiffness of the three-stage gear pair. The numerical calculation of the meshing stiffness of the three-stage gear pair refers to ISO-6336-1:2019.

Because of the helical gear coincidence degree $\varepsilon > 1$, in the meshing process, there will be multiple pairs of gear teeth meshing alternately. Therefore, the meshing stiffness of the gear pair changes periodically with the number of meshing teeth. The meshing stiffness of a gear can be approximated by Fourier series. In this paper, the first-order Fourier series is used to approximate the meshing stiffness of a gear pair $K^k(t)$[31].

$$K^k(t) = K_m^k + \Delta K_m^k \cos\left(\omega_m^k t + \varphi_m^k\right) \tag{3}$$

where $Kk\ m$ represents the meshing stiffness of the three-stage gear pair, $\Delta Kk\ m$ represents the variation amplitude of the meshing stiffness of the three-stage

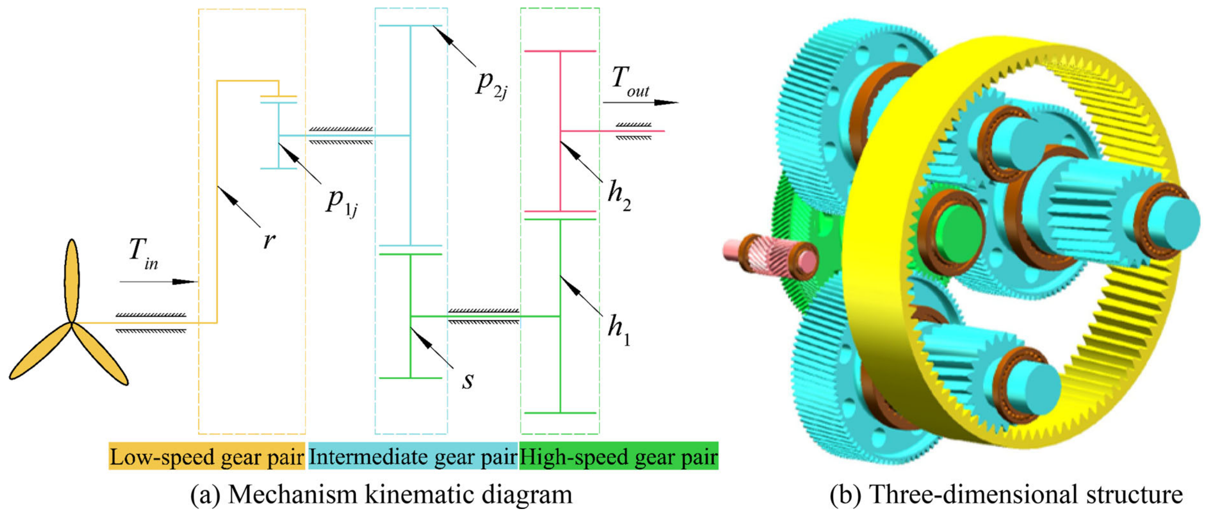

(a) Mechanism kinematic diagram (b) Three-dimensional structure

Fig. 1 NW wind power accelerator transmission structure. **a** Mechanism kinematic diagram, **b** Three-dimensional structure

Fig. 2 Followed wind speed graph in 400 s

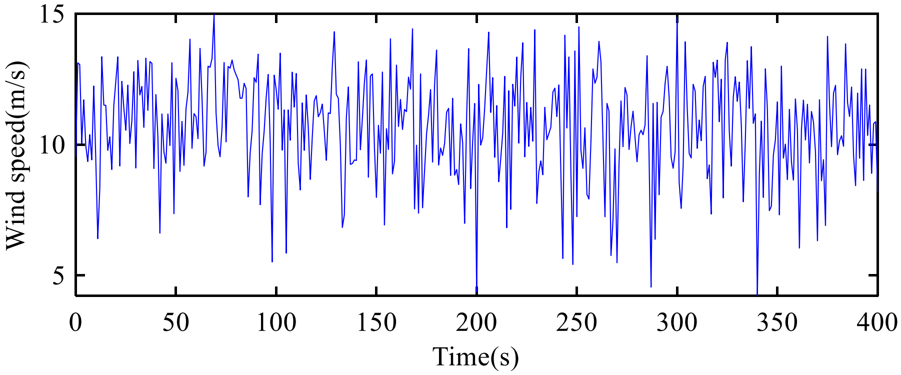

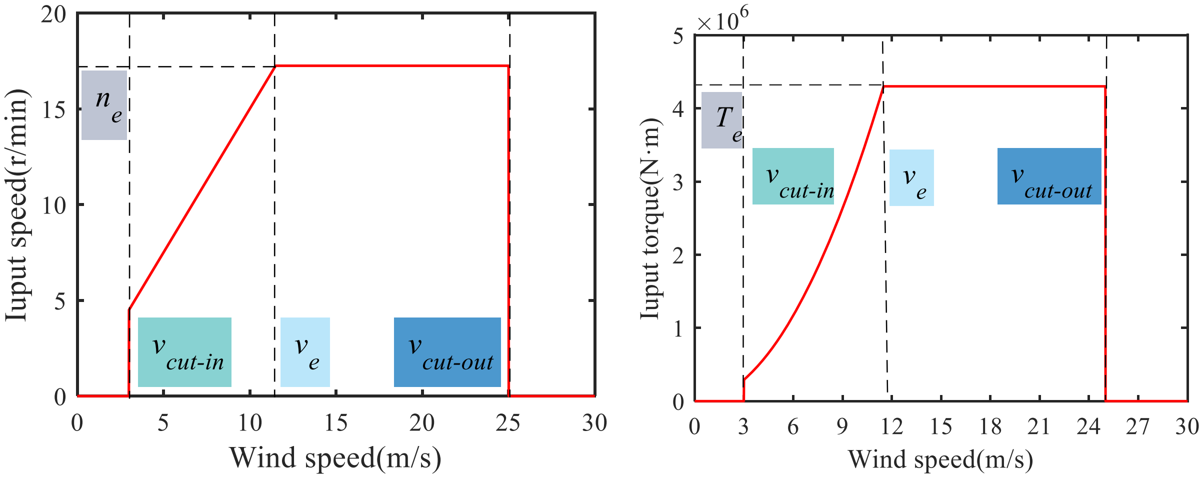

(a) Input speed (b) Input torque

Fig. 3 Variation of input speed and torque. **a** Input speed, **b** Input torque

Table 1 Basic parameters of NW wind turbine

Parameters	Value	Parameters	Value
Rated power (MW)	5	Cut-in wind speed (m/s)	3
Rated wind speed (m/s)	11.5	Cut-out wind speed (m/s)	25
Blade diameter (m)	171	Rated torque (N·m)	4.3×10^6
Blade number	3	Rated input speed (m/s)	17.3

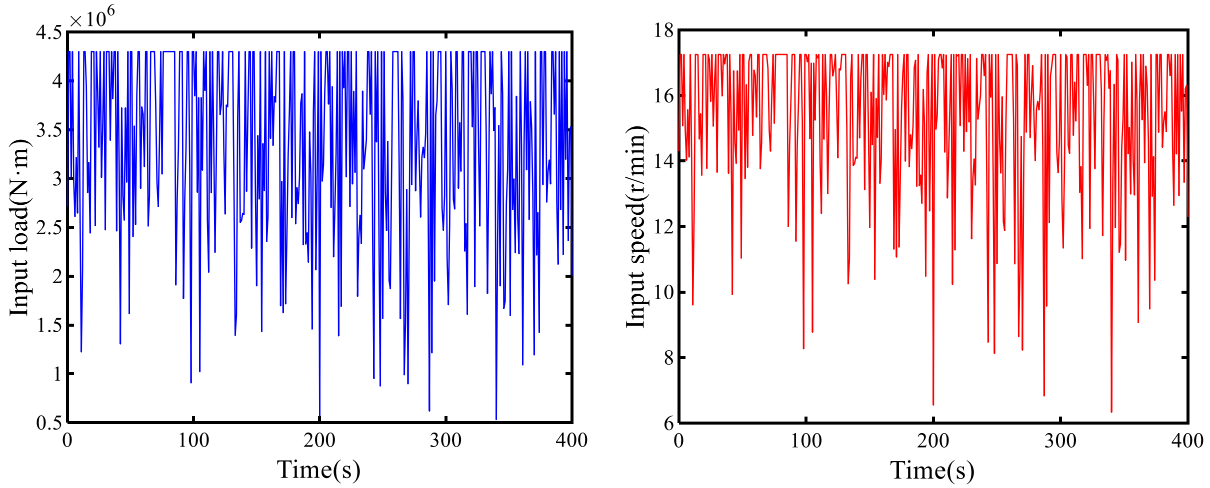

Fig. 4 Torque and speed input in 400 s

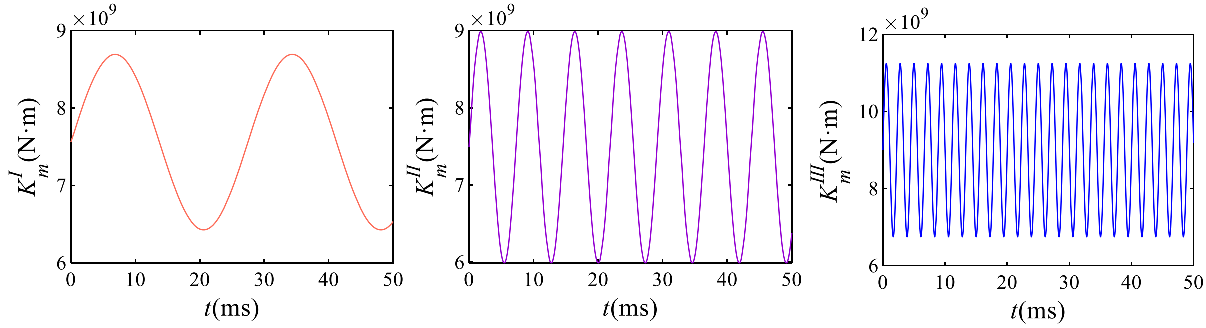

(a) Low-speed gear pair (b) Intermediate gear pair (c) High-speed gear pair

Fig. 5 Time-varying mesh stiffness of three-stage gear pair. **a** Low-speed gear pair, **b** Intermediate gear pair, **c** High-speed gear pair

gear pair, $\omega k\ m$ is the meshing frequency of the three-stage gear pair, and $\varphi k\ m$ is the phase angle of the three-stage gear pair. (k = I, II, III).

2.4 Sliding friction of tooth surface

The driving gear's meshing point goes from the tooth root to the tooth tip throughout the gear meshing operation, and its linear velocity steadily decreases. The meshing point of the driven gear moves from the tooth tip to the tooth root, and the linear velocity of the meshing point increases gradually. The sliding friction between the tooth surfaces is caused by the relative velocity between the two gears.

As shown in Fig. 6, N1N′1N2N′2 is the theoretical meshing plane of the two gears, B1B′1B2B′2 is the actual meshing plane of the two gears, A1A′1A2A′2 represents the meshing area of the gear pair, where β represents the helical angle of the helical gear, B represents the width of the gear, and p_b represents

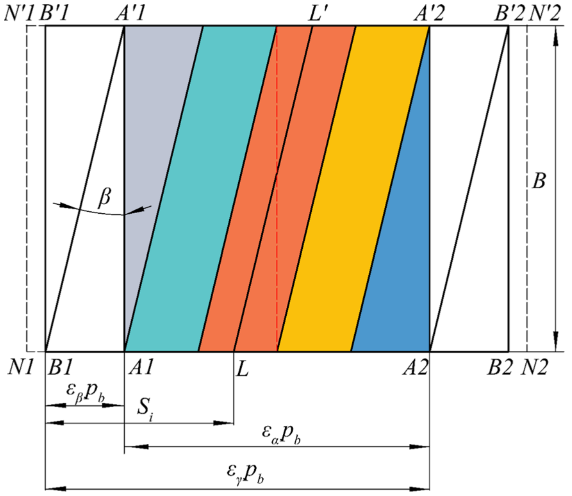

Fig. 6 Helical gear meshing area diagram. (Color figure online)

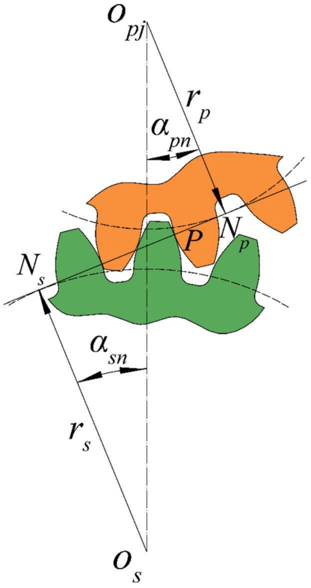

Fig. 7 End face projection of theoretical meshing plane

the pitch, ε_α represents the end coincidence degree of helical gear, ε_β represents the axial coincidence degree of helical gear, and ε_γ represents coincidence degree of helical gear. The meshing procedure of helical gear may be separated into five sections, as illustrated in Fig. 6. (1) Gray part, the actual meshing line length of the gear into a linear increase, that is, the sliding friction between the gears gradually increased, and the direction is positive. (2) Cyan part, the gear meshing line's length stays constant. (3) Orange part, the gear meshing line across the pitch line, the direction of tooth surface friction force across the pitch line changes, and the total friction is equal to the two parts minus. (4) Yellow part, the gear meshing line's length stays constant, and the direction of friction is negative. (5) Blue part, the gear meshing line's length gradually decreases, and the friction direction is negative.

The formula of gear friction is derived by taking an intermediate gear pair as an example. Figure 7 is the end face projection of the theoretical meshing plane. Equation (4) illustrates the equivalent front radius of the engagement of the ith gear tooth between the planetary gear and sun gear.

$$\begin{cases} r_{qpi}^{II} = r_{bp}^{II} \tan \alpha_t^{II} - \dfrac{1}{2} \varepsilon_\alpha^{II} p_b^{II} - B^{II} \tan \beta_b^{II} + S_i^{II} \\ r_{qsi}^{II} = r_{bs} \tan \alpha_t^{II} + \dfrac{1}{2} \varepsilon_\alpha^{II} p_b^{II} + B^{II} \tan \beta_b^{II} - S_i^{II} \end{cases} \tag{4}$$

where *r*II *bp*, r_{bs} represent the base circle radius of the planetary gear and the sun gear, B^{II} represents the width of the intermediate gear pair, and *S*II *i* is the distance from the contact line of tooth *i* to the front end. Specific expression like Eq. (5). *ω*II *p* represents the rotation angular velocity of the planetary gear. $t' = \mathrm{mod}(T_\mathrm{m})$, T_m represents meshing period of a pair of teeth.

$$S_i^{II} = \mathrm{mod}\left[\omega_p^{II} t' + 2(i-1)\pi/Z_p^{II}, 2\mathrm{ceil}(\varepsilon_\gamma^{II})\pi/Z_p^{II}\right] r_{bp}^{II} \tag{5}$$

Assuming that the gear's contact line moves to the LL′ position at a certain moment, the relative sliding velocity between the intermediate gear pairs is depicted in Eq. (6).

$$V^{II} = \omega_s r_{Ks} - \omega_p r_{Kp}^{II} \tag{6}$$

where r_{Ks} represents the radius of curvature of the end face of the gear contact point to the sun gear, *r*II *Kp* represents the radius of curvature of the end face of the gear contact point to the planetary gear. Specific expression like Eq. (7).

$$\begin{cases} r_{kp}^{II} = r_{qp}^{II} + l \sin \beta_b^{II} \\ r_{ks}^{II} = r_{qs}^{II} - l \sin \beta_b^{II} \end{cases} \tag{7}$$

where *l* represents the distance between the contact point and the gear's front face.

Since the relative sliding speed between gears is also a periodic variation related to time, the relative sliding speed is related to the lubrication state between gears. In this paper, Buckingham's semiempirical formula is used to calculate the friction coefficient between gears.

$$\mu_B^{\mathrm{II}} = 0.05e^{-0.125V^{\mathrm{II}}} + 0.002\sqrt{V^{\mathrm{II}}} \tag{8}$$

Let the relative displacement between the *i*th meshing tooth pair on the intermediate gear pair is *x*II *nji*. The friction per unit length on the meshing line is shown in Eq. (9).

$$f_{ji}^{\mathrm{II}} = \mu_B^{\mathrm{II}} \cdot k_{ji}^{\mathrm{II}} \cdot f(x_{nji}^{\mathrm{II}}, b^{\mathrm{II}}) \tag{9}$$

where *k*II *ji* is meshing stiffness per unit length on the contact line, $f(x_{nji}^{\mathrm{II}}, b^{\mathrm{II}})$ is tooth-backlash function. Specific expression like Eq. (10).

$$f(x_{nji}^{\mathrm{II}}, b^{\mathrm{II}}) = \begin{cases} x_{nji}^{\mathrm{II}} - b^{\mathrm{II}}, & x_{nji}^{\mathrm{II}} > b^{\mathrm{II}} \\ 0, & |x_{nji}^{\mathrm{II}}| \le b^{\mathrm{II}} \\ x_{nji}^{\mathrm{II}} + b^{\mathrm{II}}, & x_{nji}^{\mathrm{II}} < -b^{\mathrm{II}} \end{cases} \tag{10}$$

According to the appeal analysis, the expression of the friction force on a single tooth pair is as follows.

$$F_{ji}^{\mathrm{II}} = \begin{cases} \int_{(\varepsilon_\beta^{\mathrm{II}} p_b^{\mathrm{II}} - S_i^{\mathrm{II}})/\sin\beta_b^{\mathrm{II}}}^{B^{\mathrm{II}}/\cos\beta_b^{\mathrm{II}}} f_{ji}^{\mathrm{II}} \mathrm{d}l & S_i^{\mathrm{II}} \in \left(0, \varepsilon_\beta^{\mathrm{II}} p_b^{\mathrm{II}}\right) \\ \int_0^{B^{\mathrm{II}}/\cos\beta_b^{\mathrm{II}}} f_{ji}^{\mathrm{II}} \mathrm{d}l & S_i^{\mathrm{II}} \in \left[\varepsilon_\beta^{\mathrm{II}} p_b^{\mathrm{II}}, \frac{1}{2}\varepsilon_\alpha^{\mathrm{II}} p_b^{\mathrm{II}}\right) \\ \left(\int_0^{\left[\left(\frac{1}{2}\varepsilon_\alpha^{\mathrm{II}} + \varepsilon_\beta^{\mathrm{II}}\right)p_b^{\mathrm{II}} - S_i^{\mathrm{II}}\right]/\sin\beta_b^{\mathrm{II}}} - \int_{\left[\left(\frac{1}{2}\varepsilon_\alpha^{\mathrm{II}} + \varepsilon_\beta^{\mathrm{II}}\right)p_b^{\mathrm{II}} - S_i^{\mathrm{II}}\right]/\sin\beta_b^{\mathrm{II}}}^{B^{\mathrm{II}}/\cos\beta_b^{\mathrm{II}}} f_{ji}^{\mathrm{II}} \mathrm{d}l\right) & S_i^{\mathrm{II}} \in \left[\frac{1}{2}\varepsilon_\alpha^{\mathrm{II}} p_b^{\mathrm{II}}, \left(\frac{1}{2}\varepsilon_\alpha^{\mathrm{II}} + \varepsilon_\beta^{\mathrm{II}}\right)p_b^{\mathrm{II}}\right) \\ -\int_0^{B^{\mathrm{II}}/\cos\beta_b^{\mathrm{II}}} f_{ji}^{\mathrm{II}} \mathrm{d}l & S_i^{\mathrm{II}} \in \left[\left(\frac{1}{2}\varepsilon_\alpha^{\mathrm{II}} + \varepsilon_\beta^{\mathrm{II}}\right)p_b^{\mathrm{II}}, \varepsilon_\alpha^{\mathrm{II}} p_b^{\mathrm{II}}\right) \\ -\int_0^{(S_i^{\mathrm{II}} - \varepsilon_\gamma^{\mathrm{II}} p_b^{\mathrm{II}})/\sin\beta_b^{\mathrm{II}}} f_{ji}^{\mathrm{II}} \mathrm{d}l & S_i^{\mathrm{II}} \in \left[\varepsilon_\alpha^{\mathrm{II}} p_b^{\mathrm{II}}, \varepsilon_\gamma^{\mathrm{II}} p_b^{\mathrm{II}}\right) \\ 0 & S_i^{\mathrm{II}} \in \left[\varepsilon_\gamma^{\mathrm{II}} p_b^{\mathrm{II}}, +\infty\right) \end{cases} \tag{11}$$

The friction forces of planetary gear 2 and sun gear:

$$F_{fpi}^{\mathrm{II}} = \sum_{i=1}^{\mathrm{ceil}(\varepsilon_\gamma^{\mathrm{II}})} F_{ji}^{\mathrm{II}}, \quad F_{fs} = \sum_{j=1}^{3} F_{fpi}^{\mathrm{II}} \tag{12}$$

The friction torques on a single tooth of planetary gear 2 and sun gear:

$$M_{ji}^{\mathrm{II}} = \int f_{ji} \cdot r_{Kp}^{\mathrm{II}} \mathrm{d}l, \quad M_{sji} = \int f_{ji} \cdot r_{Ks}^{\mathrm{II}} \mathrm{d}l \tag{13}$$

The friction torques of planetary gear 2 and sun gear:

$$M_{pj}^{\mathrm{II}} = \sum_{i=1}^{\mathrm{ceil}(\varepsilon_\gamma^{\mathrm{II}})} M_{ji}^{\mathrm{II}}, \quad M_s = \sum_{i=1}^{\mathrm{ceil}(\varepsilon_\gamma^{\mathrm{II}})} M_{sji} \tag{14}$$

Similarly, the friction of inner ring gear and planetary gear 1:

$$F_{fr} = \sum_{j=1}^{3} F_{fpi}^{\mathrm{I}}, \quad F_{fpi}^{\mathrm{I}} = \sum_{i=1}^{\mathrm{ceil}(\varepsilon_\gamma^{\mathrm{I}})} F_{ji}^{\mathrm{I}} \tag{15}$$

The friction torques:

$$M_r = \sum_{i=1}^{\mathrm{ceil}(\varepsilon_\gamma^{\mathrm{I}})} M_{rji}, \quad M_{pj}^{\mathrm{I}} = \sum_{i=1}^{\mathrm{ceil}(\varepsilon_\gamma^{\mathrm{I}})} M_{ji}^{\mathrm{I}} \tag{16}$$

The friction force of herringbone gear 1 and herringbone gear 2:

$$F_{f1} = \sum_{i=1}^{\mathrm{ceil}(\varepsilon_\gamma^{\mathrm{III}})} F_{fi}^{\mathrm{I}}, \quad F_{f2} = F_{f1} \tag{17}$$

The friction torque:

$$M_1 = \sum_{i=1}^{\mathrm{ceil}(\varepsilon_\gamma^{\mathrm{III}})} M_{1i}, \quad M_2 = \sum_{i=1}^{\mathrm{ceil}(\varepsilon_\gamma^{\mathrm{III}})} M_{2i} \tag{18}$$

2.5 Time-varying support stiffness

Taking the cylindrical roller bearing as an example, the bearing force is derived. Figure 8 is a cylindrical roller-bearing model. The supporting bearing's outer ring is fastened to the bearing seat, and its inner ring is permanently coupled to the rotating shaft. The inner ring of the bearing and the center of the bearing coordinate system are aligned, and the rotary shaft and its axis OZ are aligned as well.

The bearing coordinate system's origin is at the heart of its width. The inner and outer rings and the bearing roller do not slide against one another, supposing that the bearing rollers are evenly distributed on the cage. Equation (19) displays the linear velocities v_{bi} and v_{bo} at the bearing roller's contact point with the inner and outer circular.

$$\begin{cases} v_{bi} = \omega_{bi} r_{bi} \\ v_{bo} = \omega_{bo} r_{bo} \end{cases} \tag{19}$$

where ω_{bi} and ω_{bo} are the angular velocities of the inner and outer rings. r_{bi} and r_{bo} are the radius of the bearing's inner and outer rings, respectively. ω_{bo} is equal to 0 since rigid connection of the outer ring and bearing seat.

The cage's angular velocity is equal to the bearing roller's angular velocity of revolution, which is denoted by Eq. (20)

Fig. 8 Cylindrical roller-bearing model

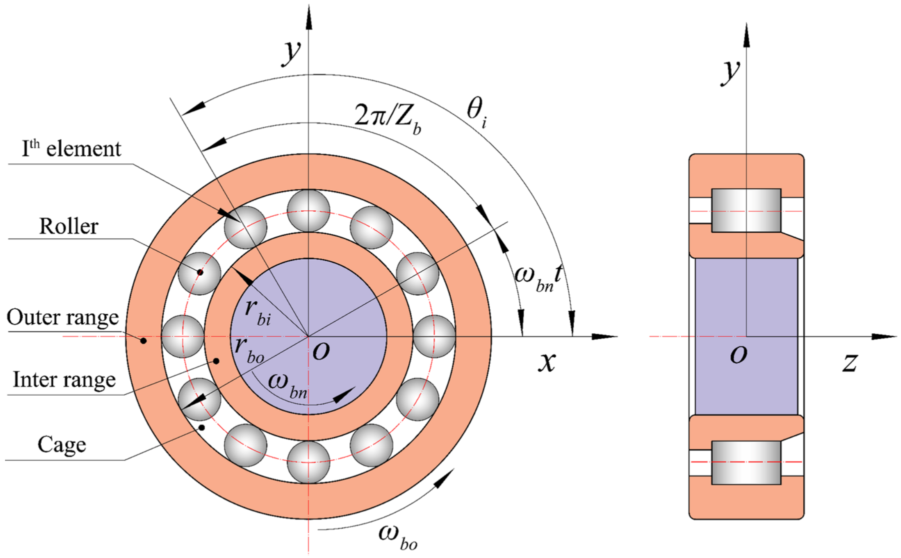

$$\omega_{bn} = \frac{v_{bi} + v_{bo}}{r_{bi} + r_{bo}} = \frac{\omega_{bi} r_{bi}}{r_{bi} + r_{bo}} \tag{20}$$

It is possible to represent the ith roller's rotational angle as a function of time t.

$$\theta_i(t) = \frac{2\pi(i-1)}{Z_b} + \omega_{bn} t \quad i = 1, 2, \ldots, Z_b \tag{21}$$

where Z_b indicates the rollers' number.

Figure 9a is the deformation diagram of the bearing rolling element, when the bearing is not forced, the inner and outer ring raceway curvature centers are O_{bi} and O_{bo}, and the radius of curvature are r_{bi} and r_{bo}. After the bearing is pressed, the center distance of the inner and outer ring raceways' curvature centers shifts from l to l'. Ignoring centrifugal force and gyroscopic moment of the rolling element, the contact angle of the rolling element and inner and outer ring raceway is equal, contact force is equal. When the bearing is not stressed, the contact angle is γ. After the bearing is stressed, the contact angle is γ'. The geometric relationship is depicted in Fig. 9b. Because the outer ring of the bearing is fixed to the cylindrical roller-bearing seat, O_{bo} and O'_{bo}'s locations coincide, and the inner ring's center of curvature shifts from O_{bi} to O'_{bi} during load, the outer ring's position is unaffected. The rolling element's axial, radial, and angular deformations are denoted by the letters δ_a, δ_r, and δ_θ. Equation (22) can be used to express the center distance between the inner and outer ring curvature centers after bearing deformation.

$$l' = \sqrt{(l \sin\gamma_i + z + r_{bo}\delta_\theta \cos\theta_i)^2 + (l\cos\gamma_i + x\cos\theta_i + y\sin\theta_i)^2} \tag{22}$$

where x, y, and z represent vibration displacements along the coordinate axis.

As a result, the rolling element's deformation can be expressed as:

$$\delta = l' - l - c \tag{23}$$

where c represents rolling bearing clearance.

Following a force-induced deformation, the rolling element's contact angle, is expressed as:

$$\tan\gamma'_i = \frac{l\sin\gamma_i + z + r_{bo}\cos\theta_i}{l\cos\gamma_i + x\cos\theta_i + y\sin\theta_i} \tag{24}$$

Considering that the positive contact pressure is generated only when $\delta > 0$, the axial and radial components of the contact force between the rolling body and the inner and outer rings are shown in Eq. (25).

$$\begin{cases} F_{ab} = K_b \delta^n \sin\gamma'_i \cdot H(\delta) \\ F_{rb} = K_b \delta^n \cos\gamma'_i \cdot H(\delta) \end{cases} \tag{25}$$

where the index n represents 3/2 for the roller bearings and 10/9 for the roller bearings, K_b stands for the support stiffness of the bearing, and H stands for the Heaviside function.

$$H(\delta) = \begin{cases} 1, & \delta > 0 \\ 0, & \delta < 0 \end{cases} \tag{26}$$

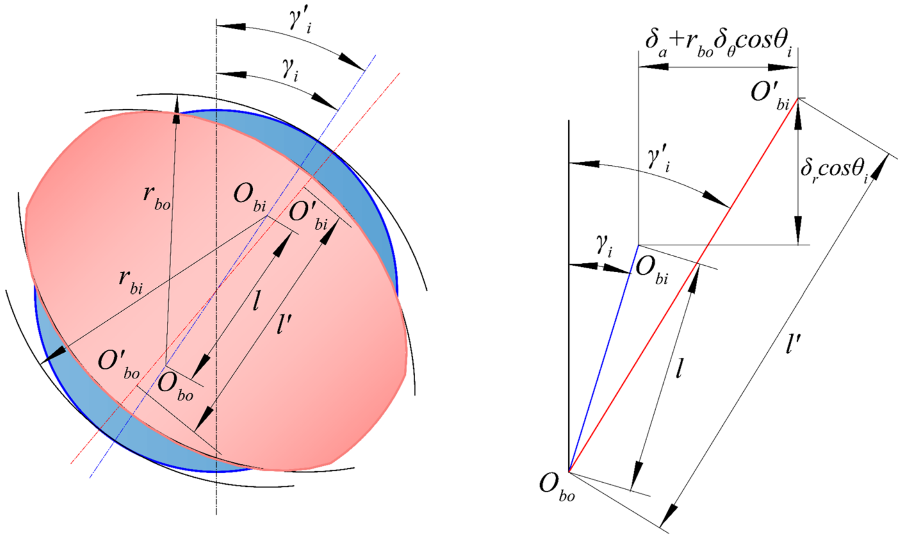

(a) Rolling element deformation diagram (b) Geometric relationship diagram

Fig. 9 Rolling deformation. **a** Rolling element deformation diagram, **b** Geometric relationship diagram

The bearing force in its coordinate system is expressed as:

$$\begin{cases} F_{bx} = \sum_{i=1}^{Z_b} F_{rb} \cos\theta_i \\ F_{by} = \sum_{i=1}^{Z_b} F_{rb} \sin\theta_i \\ F_{bz} = \sum_{i=1}^{Z_b} F_{ab} \end{cases} \tag{27}$$

2.6 Gear ring flexibility

The gear structure of the NW wind speed increaser is huge and bears the load caused by random wind speed. In this case, the internal gear ring is equivalent to a thin ring. Therefore, it is impossible to disregard the internal gear ring's flexibility. In this paper, the inner gear ring is divided into M ($M \geq 100$) segments by using the idea of discretization. The inner gear ring is regarded as a combination of M rigid bodies and M springs with a length of 0. The bending section stiffness of the ring gear is taken as the connection stiffness between the micro-segments of the ring gear (Fig. 10).

The end face diagram of the planetary gear and the micro-segment of gear ring at a certain time is shown in Fig. 11.$\varphi = \pi/M$. φ_{ri} represents the phase angle of the gear micro-segment I, $\varphi_{ri} = \omega_r t + 2\pi(i-1)/M$. Φ_j^{I} represents the meshing phase angle of participating meshing micro-segment of gear ring and planetary gear j, $\Phi_j^{\mathrm{I}} = \varphi_j^{\mathrm{I}} + \alpha_t^{\mathrm{I}}$.

The equivalent springs between the ring gear's micro-segments are projected along the x and y directions, as depicted in Fig. 11. Micro-segments centroid position of adjacent ring gear changes from $C_{r,i+1}$, $C_{r,i}$, $C_{r,i\text{-}1}$to $C'_{r,i+1}$, $C'_{r,i}$, $C'_{r,i\text{-}1}$. The relative displacement of the equivalent springs between adjacent ring gear segments along their respective x and y axes can be shown in Eq. (28).

$$\begin{cases} \Delta x_{ri} = x_{ri} - x_{ri-1} - a\cos(\xi + \varphi_{ri} + u_{ri}) + a\cos(\xi - \varphi_{ri-1} - u_{ri}) \\ \Delta y_{ri} = -y_{ri} + y_{ri-1} - a\sin(\xi + \varphi_{ri} + u_{ri}) - a\sin(\xi - \varphi_{ri-1} - u_{ri}) \end{cases} \tag{28}$$

where a is the distance between the connecting spring and the centroid of the ring gear micro-segment C_i. $a = 2r_c \sin(\varphi/2)$,$\xi = (\pi - \varphi)/2$.

2.7 Gear meshing force

The vibration displacements of all gears are projected along their respective meshing lines. Considering the transmission error, the meshing displacements of the three-stage gear pair can be obtained as shown in Eq. (29), (32), and (33), respectively.

Relative meshing displacement of participating ring micro-segment and *j*th planetary gear:

$$x_{n1} = \left[\pm u_{ri} - u_{pi}^{\mathrm{I}} - \left(x_{ri} - x_{pi}^{\mathrm{I}}\right)\sin\Phi_j^{\mathrm{I}} - \left(y_{ri} - y_{pj}^{\mathrm{I}}\right)\cos\Phi_j^{\mathrm{I}}\right]\cos\beta_b^{\mathrm{I}} + \left(z_{ri} - z_{pj}^{\mathrm{I}}\right)\sin\beta_b^{\mathrm{I}} + e^{\mathrm{I}}(t) \tag{29}$$

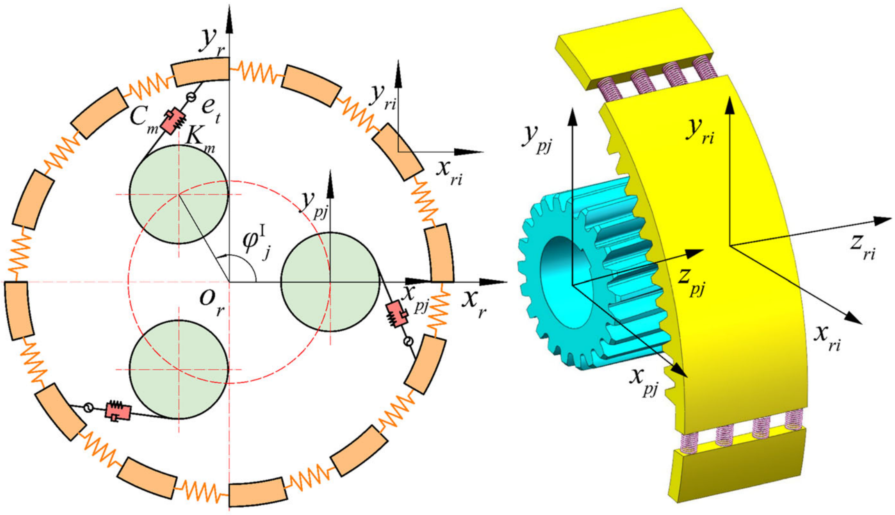

Fig.10 Schematic diagram of low-speed gear pair. **a** End face diagram, **b** Axial diagram

(a) End face diagram (b) Axial diagram

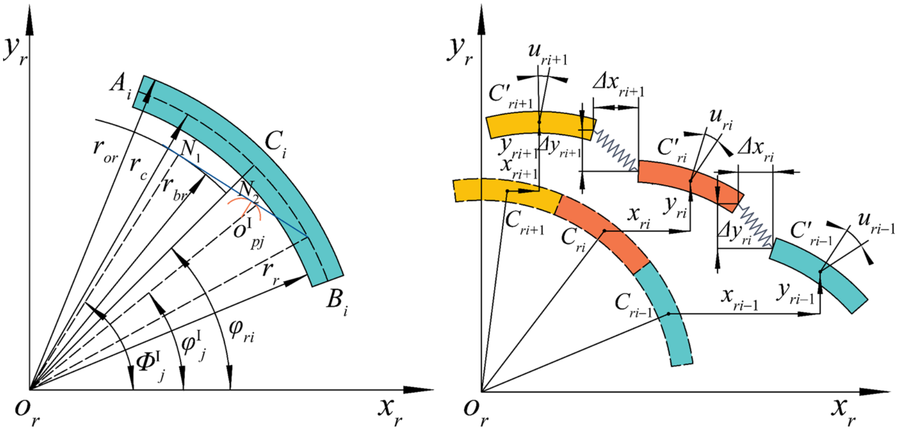

Fig.11 Geometric relation diagram of gear ring deformation. **a** Instantaneous meshing diagram, **b** Relative position diagram

(a) Instantaneous meshing diagram (b) Relative position diagram

If the action point of meshing force is on C_iB_i, Eq. (30) is satisfied.

$$\frac{\pi}{M} - \left[\varphi_{ri} - \frac{2\pi(j-1)}{N} + \arccos\left(\frac{r_{br}}{r_c}\right) - \alpha_t^{\mathrm{I}}\right] \le \frac{\pi}{M} \tag{30}$$

So, in Eq. (29), '±' takes '−,' else '±' takes '+.' When the planet gear engages with the micro-segment i, the meshing point is between A_iB_i, and Eq. (31) is satisfied.

$$\frac{\pi}{M} - \left[\varphi_{ri} - \frac{2\pi(j-1)}{N} + \arccos\left(\frac{r_{br}}{r_c}\right) - \alpha_t^{\mathrm{I}}\right] \le \frac{2\pi}{M} \tag{31}$$

Relative meshing displacement between the sun gear and the *j*th planetary gear:

$$\begin{aligned} x_{n2} = &\left[u_s - u_{pj}^{\mathrm{II}} + \left(x_s - x_{pi}^{\mathrm{II}}\right)\sin\Phi_j^{\mathrm{II}} + \left(y_s - y_{pj}^{\mathrm{II}}\right)\cos\Phi_j^{\mathrm{II}}\right] \\ &\cos\beta_b^{\mathrm{II}} + \left(z_s - z_{pj}^{\mathrm{II}}\right)\sin\beta_b^{\mathrm{II}} + e^{\mathrm{II}}(t) \end{aligned} \tag{32}$$

Relative meshing displacement of high-speed herringbone gear pair:

$$\begin{aligned} x_{n3} = &\left[u_1 - u_2 + (x_1 - x_2)\sin\alpha_t^{\mathrm{III}} + (y_1 - y_2)\cos\alpha_t^{\mathrm{III}}\right] \\ &\cos\beta_b^{\mathrm{III}} + (z_1 - z_2)\sin\beta_b^{\mathrm{III}} + e^{\mathrm{III}}(t) \end{aligned} \tag{33}$$

where $e^k(t)$ (k = I, II, III) is the static transmission error of gear pair, it can be fitted by harmonic function:

$$e^k(t) = e_a^k + e_r^k \sin(\omega_m t + \varphi_0) \tag{34}$$

where *ek a* represents the error constant, *ek r* represents the error fluctuation amplitude, ω_m is the meshing angle frequency of the gear pair, and φ_o is the phase angle.

Relative meshing displacement according to the above. The three-stage gear pair's meshing force can be written as:

$$\begin{cases} F_{mj}^{\mathrm{I}} = K_m^{\mathrm{I}} f(x_{n1}, b^{\mathrm{I}}) + C_m^{\mathrm{I}} \dot{x}_{n1} \\ F_{mj}^{\mathrm{II}} = K_m^{\mathrm{II}} f(x_{n2}, b^{\mathrm{II}}) + C_m^{\mathrm{II}} \dot{x}_{n2} \\ F_m^{\mathrm{III}} = K_m^{\mathrm{III}} f(x_{n3}, b^{\mathrm{III}}) + C_m^{\mathrm{III}} \dot{x}_{n3} \end{cases} \tag{35}$$

2.8 Dynamic model of NW wind power planetary gear system

As depicted in Fig. 12, a multi-degree-of-freedom coupled dynamic model of an NW wind power planetary gear-bearing system is created. The origin of the coordinate system coincides with the center of the internal gear ring. The *x*-axis in every coordinate system is parallel to the paper's surface from the inside out. The origin of the bearing coordinate system is the center of the support, and the *z*-axis and the axis of rotation are parallel.

The system's vibration model includes the fluctuation of random wind speed, the time-varying meshing stiffness, friction, transmission error, tooth backlash, and bearing clearance. In Fig. 12, T_{in} (t) is the input torque considering fluctuations, and T_{out} is the output torque. The support stiffness of the bearing is represented by K_{pb1}, K_{pb2}, K_{sb}, $K_{1\mathrm{b}}$, K_{21b}, and K_{22b}. The damping is represented by C_{pb1}, C_{pb2}, C_{sb}, $C_{1\mathrm{b}}$, C_{21b}, and C_{22b}.

3 System vibration differential equation

In the vibration model, the gear and the bearing are regarded as the concentrated mass and are located in the middle of their respective supports. In the transmission process of helical gear and herringbone gear pair, the meshing force can be decomposed into three directions of *x*, *y*, and *z* in the gear coordinate system. The coordinate system of the micro-segment of the inner ring gear is established in a dynamic coordinate system that rotates synchronously with the inner ring gear with its micro-segment centroid as the center. The degree of freedom of the NW wind power planetary gear-bearing system is depicted in Eq. (36).

$$\left(u_{ri}, x_{ri}, y_{ri}, z_{ri}, x_{pb1}, y_{pb1}, z_{pb1}, u_{pj}^{\mathrm{I}}, x_{pj}^{\mathrm{I}}, y_{pj}^{\mathrm{I}}, z_{pj}^{\mathrm{I}}, u_{pj}^{\mathrm{II}}, x_{pb2}, y_{pb2}, z_{pb2}, x_{pj}^{\mathrm{II}}, y_{pj}^{\mathrm{II}}, z_{pj}^{\mathrm{II}}, u_s, x_s, y_s, z_s, x_{sb}, y_{sb}, z_{sb}, u_1, x_1, y_1, z_1, x_{1\mathrm{b}}, y_{1b}, z_{1b}, u_2, x_2, y_2, x_{21\mathrm{b}}, y_{21b}, x_{22\mathrm{b}}, y_{22b}\right)^T \tag{36}$$

where *u*, *x*, *y* and *z* are the degrees of freedom of torsion, *x*-axis, *y*-axis, and *z*-axis, respectively. Subscripts *ri*, *pj*, *pb*, *s*, *sb*, 1, 1*b*, 2, 2*b* represent the *i*th micro-segment, the *j*th planetary gear, planetary gear bearing, sun gear bearing, herringbone gear 1, herringbone gear 1 bearing, herringbone gear 2, herringbone gear 2 bearing. Superscripts I II III represent three-stage gear pair respectively. According to the above model, NW wind power planetary gear-bearing system's nonlinear vibration differential equation can be created.

Inner ring gear meshing micro-segment:

$$\begin{cases} \left(\frac{I_{ri}}{r_{br}^2}\right)\frac{\mathrm{d}^2u_{ri}}{\mathrm{d}t^2}+K_{uri}u_{ri}+C_{uri}\frac{\mathrm{d}u_{ri}}{\mathrm{d}t}+\left(F_{mj}^{\mathrm{I}}r_{br}-M_{ri}\right)\cos\beta^{\mathrm{I}}+aK_e(\sin\lambda_i\Delta x_{ri} \\ \qquad +\sin\eta_i\Delta x_{ri+1}-\cos\lambda_i\Delta y_{ri}+\cos\eta_i\Delta y_{ri+1})=\frac{T_{in}}{M} \\ m_{ri}\frac{\mathrm{d}^2x_{ri}}{\mathrm{d}t^2}+K_{rix}x_{ri}+C_{rix}\frac{\mathrm{d}x_{ri}}{\mathrm{d}t}-\left(F_{mj}^{\mathrm{I}}\sin\psi_j^{\mathrm{I}}-F_{fpj}^{\mathrm{I}}\cos\psi_j^{\mathrm{I}}\right)+K_e(\Delta x_{ri}-\Delta x_{ri+1})=0 \\ m_{ri}\frac{\mathrm{d}^2y_{ri}}{\mathrm{d}t^2}+K_{riy}y_{ri}+C_{riy}\frac{\mathrm{d}y_{ri}}{\mathrm{d}t}+\left(F_{mj}^{\mathrm{I}}\cos\psi_j^{\mathrm{I}}-F_{fpj}^{\mathrm{I}}\sin\psi_j^{\mathrm{I}}\right)\cos\beta^{\mathrm{I}}-K_e(\Delta y_{ri}-\Delta y_{ri+1})=0 \\ m_{ri}\frac{\mathrm{d}^2z_{ri}}{\mathrm{d}t^2}+K_{riz}z_{ri}+C_{riz}\frac{\mathrm{d}z_{ri}}{\mathrm{d}t}+\left(F_{mj}^{\mathrm{I}}\cos\psi_j^{\mathrm{I}}-F_{fpj}^{\mathrm{I}}\sin\psi_j^{\mathrm{I}}\right)\sin\beta^{\mathrm{I}}=0 \end{cases} . \tag{37}$$

Non-meshing micro-segment of inner gear ring:

$$\begin{cases} \left(\frac{I_{ri}}{r_{br}^2}\right)\frac{\mathrm{d}^2u_{ri}}{\mathrm{d}t^2} + K_{uri}u_{ri} + C_{uri}\frac{\mathrm{d}u_{ri}}{\mathrm{d}t} + aK_e(\sin\lambda_i\Delta x_{ri} + \sin\eta_i\Delta x_{ri+1} \\ -\cos\lambda_i\Delta y_{ri} + \cos\eta_i\Delta y_{ri+1}) = \frac{T_{in}}{M} \\ m_{ri}\frac{\mathrm{d}^2x_{ri}}{\mathrm{d}t^2} + K_{rix}x_{ri} + C_{rix}\frac{\mathrm{d}x_{ri}}{\mathrm{d}t} + K_e(\Delta x_{ri} - \Delta x_{ri+1}) = 0 \\ m_{ri}\frac{\mathrm{d}^2y_{ri}}{\mathrm{d}t^2} + K_{riy}y_{ri} + C_{riy}\frac{\mathrm{d}y_{ri}}{\mathrm{d}t} - K_e(\Delta y_{ri} - \Delta y_{ri+1}) = 0 \\ m_{ri}\frac{\mathrm{d}^2z_{ri}}{\mathrm{d}t^2} + K_{riz}z_{ri} + C_{riz}\frac{\mathrm{d}z_{ri}}{\mathrm{d}t} = 0 \end{cases} . \tag{38}$$

Planetary gear bearing 1:

$$\begin{cases} m_{pb1}\frac{\mathrm{d}^2x_{pb1}}{\mathrm{d}t^2}+K_{px}\left(x_{pb1}-x_{pj}^{\mathrm{I}}\right)+C_{px}\frac{\mathrm{d}\left(x_{pb1}-x_{pj}^{\mathrm{I}}\right)}{\mathrm{d}t}+C_{pb1}\frac{\mathrm{d}x_{pb1}}{\mathrm{d}t}=-F_{pb1x} \\ m_{pb1}\frac{\mathrm{d}^2y_{pb1}}{\mathrm{d}t^2}+K_{py}\left(y_{pb1}-y_{pj}^{\mathrm{I}}\right)+C_{py}\frac{\mathrm{d}\left(y_{pb1}-y_{pj}^{\mathrm{I}}\right)}{\mathrm{d}t}+C_{pb1}\frac{\mathrm{d}y_{pb1}}{\mathrm{d}t}=-F_{pb1y}-m_{pb1}g \\ m_{pb1}\frac{\mathrm{d}^2z_{pb1}}{\mathrm{d}t^2}+K_{pz}\left(z_{pb1}-z_{pj}^{\mathrm{I}}\right)+C_{pz}\frac{\mathrm{d}\left(z_{pb1}-z_{pj}^{\mathrm{I}}\right)}{\mathrm{d}t}+C_{pb1}\frac{\mathrm{d}z_{pb1}}{\mathrm{d}t}=-F_{pb1z} \end{cases} \tag{39}$$

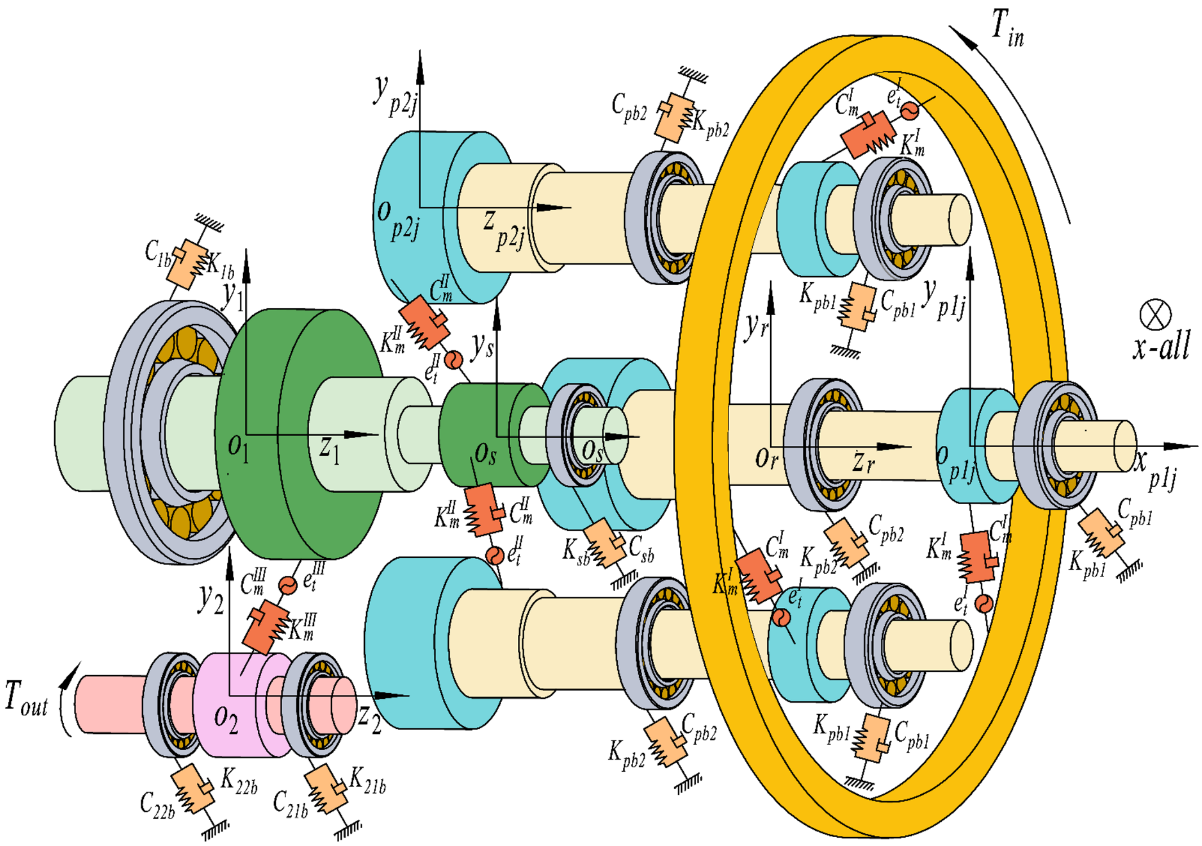

Fig. 12 Dynamic model of NW wind power planetary gear system

Internal meshing planetary gear:

$$\begin{cases}\left[\frac{I_p^{\mathrm{I}}}{(r_{bp}^{\mathrm{I}})^2}\right]\frac{\mathrm{d}^2u_{pj}^{\mathrm{I}}}{\mathrm{d}t^2}+K_{up}^{\mathrm{I}}\left(u_{pj}^{\mathrm{I}}-u_{pj}^{\mathrm{I}}\frac{r_{bp}^{\mathrm{I}}}{r_{bp}^{\mathrm{II}}}\right)+C_{up}^{\mathrm{I}}\frac{\mathrm{d}\left(u_{pj}^{\mathrm{I}}-u_{pj}^{\mathrm{I}}r_{bp}^{\mathrm{I}}/r_{bp}^{\mathrm{II}}\right)}{\mathrm{d}t}-\left(F_{mj}^{\mathrm{I}}r_{bp}^{\mathrm{I}}-M_{pj}^{\mathrm{I}}\right)\cos\beta^{\mathrm{I}}=0\\ m_p^{\mathrm{I}}\frac{\mathrm{d}^2x_{pj}^{\mathrm{I}}}{\mathrm{d}t^2}+K_{px}\left(2x_{pj}^{\mathrm{I}}-x_{pb1}-x_{pb2}\right)+C_{px}\frac{\mathrm{d}\left(2x_{pj}^{\mathrm{I}}-x_{pb1}-x_{pb2}\right)}{\mathrm{d}t}+\left(F_{mj}^{\mathrm{I}}\sin\psi_j^{\mathrm{I}}-F_{fpj}^{\mathrm{I}}\cos\psi_j^{\mathrm{I}}\right)=0\\ m_p^{\mathrm{I}}\frac{\mathrm{d}^2y_{pj}^{\mathrm{I}}}{\mathrm{d}t^2}+K_{py}\left(2y_{pj}^{\mathrm{I}}-y_{pb1}-y_{pb2}\right)+C_{py}\frac{\mathrm{d}\left(2y_{pj}^{\mathrm{I}}-y_{pb1}-y_{pb2}\right)}{\mathrm{d}t}-\left(F_{mj}^{\mathrm{I}}\cos\psi_j^{\mathrm{I}}-F_{fpj}^{\mathrm{I}}\sin\psi_j^{\mathrm{I}}\right)\cos\beta^{\mathrm{I}}=-m_p^{\mathrm{I}}g\\ m_p^{\mathrm{I}}\frac{\mathrm{d}^2z_{pj}^{\mathrm{I}}}{\mathrm{d}t^2}+K_{pz}\left(2z_{pj}^{\mathrm{I}}-z_{pb1}-z_{pb2}\right)+C_{pz}\frac{\mathrm{d}\left(2z_{pj}^{\mathrm{I}}-z_{pb1}-z_{pb2}\right)}{\mathrm{d}t}-\left(F_{mj}^{\mathrm{I}}\cos\psi_j^{\mathrm{I}}-F_{fpj}^{\mathrm{I}}\sin\psi_j^{\mathrm{I}}\right)\sin\beta^{\mathrm{I}}=0\end{cases} \tag{40}$$

Planetary gear bearing 2:

$$\begin{cases}m_{pb2}\frac{\mathrm{d}^2x_{pb2}}{\mathrm{d}t^2}+K_{px}\left(2x_{pb2}-x_{pj}^{\mathrm{I}}-x_{pj}^{\mathrm{II}}\right)+C_{px}\frac{\mathrm{d}\left(2x_{pb2}-x_{pj}^{\mathrm{I}}-x_{pj}^{\mathrm{II}}\right)}{\mathrm{d}t}+C_{pb2}\frac{\mathrm{d}x_{pb2}}{\mathrm{d}t}=-F_{pb2x}\\ m_{pb2}\frac{\mathrm{d}^2y_{pb2}}{\mathrm{d}t^2}+K_{py}\left(2y_{pb2}-y_{pj}^{\mathrm{I}}-y_{pj}^{\mathrm{II}}\right)+C_{py}\frac{\mathrm{d}\left(2y_{pb2}-y_{pj}^{\mathrm{I}}-y_{pj}^{\mathrm{II}}\right)}{\mathrm{d}t}+C_{pb2}\frac{\mathrm{d}y_{pb2}}{\mathrm{d}t}=-F_{pb2y}-m_{pb2}g\\ m_{pb2}\frac{\mathrm{d}^2z_{pb2}}{\mathrm{d}t^2}+K_{pz}\left(2z_{pb2}-z_{pj}^{\mathrm{I}}-z_{pj}^{\mathrm{II}}\right)+C_{pz}\frac{\mathrm{d}\left(2z_{pb2}-z_{pj}^{\mathrm{I}}-z_{pj}^{\mathrm{II}}\right)}{\mathrm{d}t}+C_{pb2}\frac{\mathrm{d}z_{pb2}}{\mathrm{d}t}=-F_{pb2z}\end{cases} \tag{41}$$

External meshing planetary gear:

$$\begin{cases}\left[\frac{I_p^{\mathrm{II}}}{(r_{bp}^{\mathrm{II}})^2}\right]\frac{\mathrm{d}^2u_{pj}^{\mathrm{II}}}{\mathrm{d}t^2}+K_{up}^{\mathrm{II}}\left(u_{pj}^{\mathrm{II}}-u_{pj}^{\mathrm{I}}\frac{r_{bp}^{\mathrm{II}}}{r_{bp}^{\mathrm{I}}}\right)+C_{up}^{\mathrm{II}}\frac{\mathrm{d}\left(u_{pj}^{\mathrm{II}}-u_{pj}^{\mathrm{I}}r_{bp}^{\mathrm{II}}/r_{bp}^{\mathrm{I}}\right)}{\mathrm{d}t}+\left(F_{mj}^{\mathrm{II}}r_{bp}^{\mathrm{II}}-M_{pj}^{\mathrm{II}}\right)\cos\beta^{\mathrm{II}}=0\\ m_p^{\mathrm{II}}\frac{\mathrm{d}^2x_{pj}^{\mathrm{II}}}{\mathrm{d}t^2}+K_{px}\left(x_{pj}^{\mathrm{II}}-x_{pb2}\right)+C_{px}\frac{\mathrm{d}\left(x_{pj}^{\mathrm{II}}-x_{pb2}\right)}{\mathrm{d}t}-\left(F_{mj}^{\mathrm{II}}\sin\psi_j^{\mathrm{II}}-F_{fpj}^{\mathrm{II}}\cos\psi_j^{\mathrm{II}}\right)=0\\ m_p^{\mathrm{II}}\frac{\mathrm{d}^2y_{pj}^{\mathrm{II}}}{\mathrm{d}t^2}+K_{py}\left(y_{pj}^{\mathrm{II}}-y_{pb2}\right)+C_{py}\frac{\mathrm{d}\left(y_{pj}^{\mathrm{II}}-y_{pb2}\right)}{\mathrm{d}t}-\left(F_{mj}^{\mathrm{II}}\cos\psi_j^{\mathrm{II}}-F_{fpj}^{\mathrm{II}}\sin\psi_j^{\mathrm{II}}\right)\cos\beta^{\mathrm{II}}=0\\ m_p^{\mathrm{II}}\frac{\mathrm{d}^2z_{pj}^{\mathrm{II}}}{\mathrm{d}t^2}+K_{pz}\left(z_{pj}^{\mathrm{II}}-z_{pb2}\right)+C_{pz}\frac{\mathrm{d}\left(z_{pj}^{\mathrm{II}}-z_{pb2}\right)}{\mathrm{d}t}+\left(F_{mj}^{\mathrm{II}}\cos\psi_j^{\mathrm{II}}-F_{fpj}^{\mathrm{II}}\sin\psi_j^{\mathrm{II}}\right)\sin\beta^{\mathrm{II}}=0\end{cases} \tag{42}$$

Sun gear bearing 1:

$$\begin{cases}m_{sb}\frac{\mathrm{d}^2x_{sb}}{\mathrm{d}t^2}+K_{sx}(x_{sb}-x_s)+C_{sx}\frac{\mathrm{d}(x_{sb}-x_s)}{\mathrm{d}t}+C_{sb}\frac{\mathrm{d}x_{sb}}{\mathrm{d}t}=-F_{sbx}\\ m_{sb}\frac{\mathrm{d}^2y_{sb}}{\mathrm{d}t^2}+K_{sy}(y_{sb}-y_s)+C_{sy}\frac{\mathrm{d}(y_{sb}-y_s)}{\mathrm{d}t}+C_{sb}\frac{\mathrm{d}y_{sb}}{\mathrm{d}t}=-F_{sby}-m_{sb}g\\ m_{sb}\frac{\mathrm{d}^2z_{sb}}{\mathrm{d}t^2}+K_{sz}(z_{sb}-z_s)+C_{sz}\frac{\mathrm{d}(z_{sb}-z_s)}{\mathrm{d}t}+C_{sb}\frac{\mathrm{d}z_{sb}}{\mathrm{d}t}=-F_{sbz}\end{cases} \tag{43}$$

Sun gear:

$$\begin{cases}\left(\frac{I_s}{r_{bs}^2}\right)\frac{\mathrm{d}^2u_s}{\mathrm{d}t^2}+K_{us}\left(u_s-u_1\frac{r_{bs}}{r_1}\right)+C_{us}\frac{\mathrm{d}(u_s-u_1r_{bs}/r_1)}{\mathrm{d}t}-\sum_{j=1}^{3}\left(F_{mj}^{\mathrm{II}}r_{bs}-M_s\right)\cos\beta^{\mathrm{II}}=0\\ m_s\frac{\mathrm{d}^2x_s}{\mathrm{d}t^2}+K_{sx}(2x_s-x_1-x_{sb})+C_{sx}\frac{\mathrm{d}(2x_s-x_1-x_{sb})}{\mathrm{d}t}+\sum_{j=1}^{3}\left(F_{mj}^{\mathrm{II}}\sin\psi_j^{\mathrm{II}}-F_{fsj}^{\mathrm{II}}\cos\psi_j^{\mathrm{II}}\right)=0\\ m_s\frac{\mathrm{d}^2y_s}{\mathrm{d}t^2}+K_{sy}(2y_s-y_1-y_{sb})+C_{sy}\frac{\mathrm{d}(2y_s-y_1-y_{sb})}{\mathrm{d}t}+\sum_{j=1}^{3}\left(F_{mj}^{\mathrm{II}}\cos\psi_j^{\mathrm{II}}-F_{fsj}^{\mathrm{II}}\sin\psi_j^{\mathrm{II}}\right)\cos\beta^{\mathrm{II}}=-m_sg\\ m_s\frac{\mathrm{d}^2z_s}{\mathrm{d}t^2}+K_{sz}(2z_s-z_1-z_{sb})+C_{sz}\frac{\mathrm{d}(2z_s-z_1-z_{sb})}{\mathrm{d}t}-\sum_{j=1}^{3}\left(F_{mj}^{\mathrm{II}}\cos\psi_j^{\mathrm{II}}-F_{fsj}^{\mathrm{II}}\sin\psi_j^{\mathrm{II}}\right)\sin\beta^{\mathrm{II}}=0\end{cases} \tag{44}$$

Herringbone Gear 1:

$$\begin{cases}\left(\frac{I_1}{r_{b1}^2}\right)\frac{\mathrm{d}^2u_1}{\mathrm{d}t^2}+K_{u1}\left(u_1-u_s\frac{r_{b1}}{r_{bs}}\right)+C_{u1}\frac{\mathrm{d}(u_1-u_sr_{bs}/r_1)}{\mathrm{d}t}+(F_m^{\mathrm{III}}r_{b1}-M_1)\cos\beta^{\mathrm{III}}\\ m_1\frac{\mathrm{d}^2x_1}{\mathrm{d}t^2}+K_{sx}(2x_1-x_s-x_{1b})+C_{sx}\frac{\mathrm{d}(2x_1-x_s-x_{1b})}{\mathrm{d}t}-\left(F_m^{\mathrm{III}}\sin\alpha_n^{\mathrm{III}}-F_f^{\mathrm{III}}\cos\alpha_n^{\mathrm{III}}\right)=0\\ m_1\frac{\mathrm{d}^2y_1}{\mathrm{d}t^2}+K_{sy}(2y_1-y_s-y_{1b})+C_{sy}\frac{\mathrm{d}(2y_1-y_s-y_{1b})}{\mathrm{d}t}+\left(F_m^{\mathrm{III}}\cos\alpha_n^{\mathrm{III}}-F_f^{\mathrm{III}}\sin\alpha_n^{\mathrm{III}}\right)\cos\beta^{\mathrm{III}}=-m_1g\\ m_1\frac{\mathrm{d}^2z_1}{\mathrm{d}t^2}+K_{sz}(2z_1-z_s-z_{1b})+C_{sz}\frac{\mathrm{d}(2z_1-z_s-z_{1b})}{\mathrm{d}t}=0\end{cases} \tag{45}$$

Herringbone gear bearing 1:

$$\begin{cases}m_{1b}\frac{\mathrm{d}^2x_{1b}}{\mathrm{d}t^2}+K_{sx}(x_{1b}-x_1)+C_{sx}\frac{\mathrm{d}(x_{1b}-x_1)}{\mathrm{d}t}+C_{1b}\frac{\mathrm{d}x_{1b}}{\mathrm{d}t}=-F_{1bx}\\ m_{1b}\frac{\mathrm{d}^2y_{1b}}{\mathrm{d}t^2}+K_{sy}(y_{1b}-y_1)+C_{sy}\frac{\mathrm{d}(y_{1b}-y_1)}{\mathrm{d}t}+C_{1b}\frac{\mathrm{d}y_{1b}}{\mathrm{d}t}=-F_{1by}-m_{1b}g\\ m_{1b}\frac{\mathrm{d}^2z_{1b}}{\mathrm{d}t^2}+K_{sz}(z_{1b}-z_1)+C_{sz}\frac{\mathrm{d}(z_{1b}-z_1)}{\mathrm{d}t}+C_{1b}\frac{\mathrm{d}z_{1b}}{\mathrm{d}t}=-F_{1bz}\end{cases} \tag{46}$$

Herringbone Gear 2:

$$\begin{cases}\left(\frac{I_2}{r_{b2}^2}\right)\frac{\mathrm{d}^2u_2}{\mathrm{d}t^2}+K_{u2}u_2+C_{u2}\frac{\mathrm{d}u_2}{\mathrm{d}t}-(F_m^{\mathrm{III}}r_{b2}-M_2)\cos\beta^{\mathrm{III}}=T_{out}\\ m_2\frac{\mathrm{d}^2x_2}{\mathrm{d}t^2}+K_{2x}(2x_2-x_{21b}-x_{22b})+C_{2x}\frac{\mathrm{d}(2x_2-x_{21b}-x_{22b})}{\mathrm{d}t}+\left(F_m^{\mathrm{III}}\sin\alpha_n^{\mathrm{III}}-F_f^{\mathrm{III}}\cos\alpha_n^{\mathrm{III}}\right)=0\\ m_2\frac{\mathrm{d}^2y_2}{\mathrm{d}t^2}+K_{2y}(2y_2-y_{21b}-y_{22b})+C_{2y}\frac{\mathrm{d}(2y_2-y_{21b}-y_{22b})}{\mathrm{d}t}-\left(F_m^{\mathrm{III}}\cos\alpha_n^{\mathrm{III}}-F_f^{\mathrm{III}}\sin\alpha_n^{\mathrm{III}}\right)\cos\beta^{\mathrm{III}}=0\end{cases} \tag{47}$$

Herringbone gear bearing 21:

$$\begin{cases}m_{21b}\frac{\mathrm{d}^2x_{21b}}{\mathrm{d}t^2}+K_{2x}(x_{21b}-x_2)+C_{2x}\frac{\mathrm{d}(x_{21b}-x_2)}{\mathrm{d}t}+C_{21b}\frac{\mathrm{d}x_{21b}}{\mathrm{d}t}=-F_{21bx}\\ m_{21b}\frac{\mathrm{d}^2y_{21b}}{\mathrm{d}t^2}+K_{2y}(y_{21b}-y_2)+C_{2y}\frac{\mathrm{d}(y_{21b}-y_2)}{\mathrm{d}t}+C_{21b}\frac{\mathrm{d}y_{21b}}{\mathrm{d}t}=-F_{21by}-m_{21b}g\end{cases} \tag{48}$$

Herringbone gear bearing 22:

$$\begin{cases}m_{22b}\frac{\mathrm{d}^2x_{22b}}{\mathrm{d}t^2}+K_{2x}(x_{22b}-x_2)+C_{2x}\frac{\mathrm{d}(x_{22b}-x_2)}{\mathrm{d}t}+C_{22b}\frac{\mathrm{d}x_{22b}}{\mathrm{d}t}=-F_{22bx}\\ m_{22b}\frac{\mathrm{d}^2y_{22b}}{\mathrm{d}t^2}+K_{2y}(y_{22b}-y_2)+C_{2y}\frac{\mathrm{d}(y_{22b}-y_2)}{\mathrm{d}t}+C_{22b}\frac{\mathrm{d}y_{22b}}{\mathrm{d}t}=-F_{22by}-m_{22b}g\end{cases} \tag{49}$$

3.1 Nondimensionalization

The vibration differential equation of the NW gear speed-up box contains a variety of physical parameters, and the order of magnitude of the physical parameters varies greatly. In order to avoid the calculation time being too long, the calculation failure, and so on, the system differential equations are dimensionless. The natural frequency $\omega_n=\sqrt{K_{m2}/M_{e2}}$ of the intermediate gear pair for the NW wind turbine gearbox is time scale. Displacement scale with half-backlash of intermediate gear pair.

Inner ring gear meshing micro-segment:

$$\begin{cases}\frac{\mathrm{d}^2\overline{u}_{ri}}{\mathrm{d}\tau^2}+k_{uri}\overline{u}_{ri}+2\zeta_{uri}\frac{\mathrm{d}\overline{u}_{ri}}{\mathrm{d}\tau}+(\overline{f}_{mjr}^{\mathrm{I}}r_{br}-\overline{M}_{ri})\cos\beta^{\mathrm{I}}+ak_e(\sin\lambda_i\Delta\overline{x}_{ri}+\sin\eta_i\Delta\overline{x}_{ri+1}\\ -\cos\lambda_i\Delta\overline{y}_{ri}+\cos\eta_i\Delta\overline{y}_{ri+1})=\frac{t_{in}}{M}\\ \frac{\mathrm{d}^2\overline{x}_{ri}}{\mathrm{d}\tau^2}+k_{rix}\overline{x}_{ri}+2\zeta_{rix}\frac{\mathrm{d}\overline{x}_{ri}}{\mathrm{d}\tau}-\left(f_{mjr}^{\mathrm{I}}\sin\psi_j^{\mathrm{I}}-f_{fpjr}^{\mathrm{I}}\cos\psi_j^{\mathrm{I}}\right)+k_e(\Delta\overline{x}_{ri}-\Delta\overline{x}_{ri+1})=0\\ \frac{\mathrm{d}^2\overline{y}_{ri}}{\mathrm{d}\tau^2}+k_{riy}\overline{y}_{ri}+2\zeta_{riy}\frac{\mathrm{d}\overline{y}_{ri}}{\mathrm{d}\tau}+\left(f_{mjr}^{\mathrm{I}}\cos\psi_j^{\mathrm{I}}-f_{fpjr}^{\mathrm{I}}\sin\psi_j^{\mathrm{I}}\right)\cos\beta^{\mathrm{I}}-k_e(\Delta\overline{y}_{ri}-\Delta\overline{y}_{ri+1})=-f_g\\ \frac{\mathrm{d}^2\overline{z}_{ri}}{\mathrm{d}\tau^2}+k_{riz}\overline{z}_{ri}+2\zeta_{riz}\frac{\mathrm{d}\overline{z}_{ri}}{\mathrm{d}\tau}+\left(f_{mjr}^{\mathrm{I}}\cos\psi_j^{\mathrm{I}}-f_{fpjr}^{\mathrm{I}}\sin\psi_j^{\mathrm{I}}\right)\sin\beta^{\mathrm{I}}=0\end{cases}. \tag{50}$$

Non-meshing micro-segment of inner gear ring:

$$\begin{cases}\frac{\mathrm{d}^2\overline{u}_{ri}}{\mathrm{d}\tau^2}+k_{uri}\overline{u}_{ri}+2\zeta_{uri}\frac{\mathrm{d}\overline{u}_{ri}}{\mathrm{d}\tau}+ak_e(\sin\lambda_i\Delta\overline{x}_{ri}+\sin\eta_i\Delta\overline{x}_{ri+1}\\ -\cos\lambda_i\Delta\overline{y}_{ri}+\cos\eta_i\Delta\overline{y}_{ri+1})=\frac{t_{in}}{M}\\ \frac{\mathrm{d}^2\overline{x}_{ri}}{\mathrm{d}\tau^2}+k_{rix}\overline{x}_{ri}+2\zeta_{rix}\frac{\mathrm{d}\overline{x}_{ri}}{\mathrm{d}\tau}+K_e(\Delta\overline{x}_{ri}-\Delta\overline{x}_{ri+1})=0\\ \frac{\mathrm{d}^2\overline{y}_{ri}}{\mathrm{d}\tau^2}+k_{riy}\overline{y}_{ri}+2\zeta_{riy}\frac{\mathrm{d}\overline{y}_{ri}}{\mathrm{d}\tau}-k_e(\Delta\overline{y}_{ri}-\Delta\overline{y}_{ri+1})=-f_g\\ \frac{\mathrm{d}^2\overline{z}_{ri}}{\mathrm{d}\tau^2}+k_{riz}\overline{z}_{ri}+2\zeta_{riz}\frac{\mathrm{d}\overline{z}_{ri}}{\mathrm{d}\tau}=0\end{cases}. \tag{51}$$

Planetary gear bearing 1:

$$\begin{cases}\frac{\mathrm{d}^2\overline{x}_{pb1}}{\mathrm{d}\tau^2}+k_{ppb1x}(\overline{x}_{pb1}-\overline{x}_{pj}^{\mathrm{I}})+2\zeta_{ppb1x}\frac{\mathrm{d}(\overline{x}_{pb1}-\overline{x}_{pj}^{\mathrm{I}})}{\mathrm{d}\tau}+2\zeta_{pb1}\frac{\mathrm{d}\overline{x}_{pb1}}{\mathrm{d}\tau}=-f_{pb1x}\\ \frac{\mathrm{d}^2\overline{y}_{pb1}}{\mathrm{d}\tau^2}+k_{ppb1y}(\overline{y}_{pb1}-\overline{y}_{pj}^{\mathrm{I}})+2\zeta_{pp1by}\frac{\mathrm{d}(\overline{y}_{pb1}-\overline{y}_{pj}^{\mathrm{I}})}{\mathrm{d}\tau}+2\zeta_{pb1}\frac{\mathrm{d}\overline{y}_{pb1}}{\mathrm{d}\tau}=-f_{pb1y}-f_g\\ \frac{\mathrm{d}^2\overline{z}_{pb1}}{\mathrm{d}\tau^2}+k_{ppb1z}(\overline{z}_{pb1}-\overline{z}_{pj}^{\mathrm{I}})+2\zeta_{ppb1z}\frac{\mathrm{d}(\overline{z}_{pb1}-\overline{z}_{pj}^{\mathrm{I}})}{\mathrm{d}\tau}+2\zeta_{pb1}\frac{\mathrm{d}\overline{z}_{pb1}}{\mathrm{d}\tau}=-f_{pb1z}\end{cases} \tag{52}$$

Internal meshing planetary gear:

$$\begin{cases}\frac{\mathrm{d}^2\overline{u}_{pj}^{\mathrm{I}}}{\mathrm{d}\tau^2}+k_{up}^{\mathrm{I}}\left(\overline{u}_{pj}^{\mathrm{I}}-\overline{u}_{pj}^{\mathrm{I}}\frac{r_{bp}^{\mathrm{I}}}{r_{bp}^{\mathrm{II}}}\right)+2\zeta_{up}^{\mathrm{I}}\frac{\mathrm{d}\left(\overline{u}_{pj}^{\mathrm{I}}-\overline{u}_{pj}^{\mathrm{I}}r_{bp}^{\mathrm{I}}/r_{bp}^{\mathrm{II}}\right)}{\mathrm{d}\tau}-\left(f_{mjpj}^{\mathrm{I}}r_{bp}^{\mathrm{I}}-\overline{M}_{pj}^{\mathrm{I}}\right)\cos\beta^{\mathrm{I}}=0\\ \frac{\mathrm{d}^2\overline{x}_{pj}^{\mathrm{I}}}{\mathrm{d}\tau^2}+k_{ppjx}^{\mathrm{I}}\left(2\overline{x}_{pj}^{\mathrm{I}}-\overline{x}_{pb1}-\overline{x}_{pb2}\right)+2\zeta_{ppjx}^{\mathrm{I}}\frac{\mathrm{d}\left(2\overline{x}_{pj}^{\mathrm{I}}-\overline{x}_{pb1}-\overline{x}_{pb2}\right)}{\mathrm{d}\tau}+\left(f_{mjpj}^{\mathrm{I}}\sin\psi_j^{\mathrm{I}}-f_{fpj}^{\mathrm{I}}\cos\psi_j^{\mathrm{I}}\right)=0\\ \frac{\mathrm{d}^2\overline{y}_{pj}^{\mathrm{I}}}{\mathrm{d}\tau^2}+k_{ppjy}^{\mathrm{I}}\left(2\overline{y}_{pj}^{\mathrm{I}}-\overline{y}_{pb1}-\overline{y}_{pb2}\right)+2\zeta_{ppjy}^{\mathrm{I}}\frac{\mathrm{d}\left(2\overline{y}_{pj}^{\mathrm{I}}-\overline{y}_{pb1}-\overline{y}_{pb2}\right)}{\mathrm{d}\tau}-\left(f_{mjpj}^{\mathrm{I}}\cos\psi_j^{\mathrm{I}}-f_{fpj}^{\mathrm{I}}\sin\psi_j^{\mathrm{I}}\right)\cos\beta^{\mathrm{I}}=0\\ \frac{\mathrm{d}^2\overline{z}_{pj}^{\mathrm{I}}}{\mathrm{d}\tau^2}+k_{ppjz}^{\mathrm{I}}\left(2\overline{z}_{pj}^{\mathrm{I}}-\overline{z}_{pb1}-\overline{z}_{pb2}\right)+2\zeta_{ppjz}^{\mathrm{I}}\frac{\mathrm{d}\left(2\overline{z}_{pj}^{\mathrm{I}}-\overline{z}_{pb1}-\overline{z}_{pb2}\right)}{\mathrm{d}\tau}-\left(f_{mjpj}^{\mathrm{I}}\cos\psi_j^{\mathrm{I}}-f_{fpj}^{\mathrm{I}}\sin\psi_j^{\mathrm{I}}\right)\sin\beta^{\mathrm{I}}=0\end{cases} \tag{53}$$

Planetary gear bearing 2:

$$\begin{cases}\dfrac{\mathrm{d}^2\overline{x}_{pb2}}{\mathrm{d}\tau^2}+k_{ppb2x}\left(2\overline{x}_{pb2}-\overline{x}^{\mathrm{I}}_{pj}-\overline{x}^{\mathrm{II}}_{pj}\right)+2\zeta_{ppb2x}\dfrac{\mathrm{d}\left(2\overline{x}_{pb2}-\overline{x}^{\mathrm{I}}_{pj}-\overline{x}^{\mathrm{II}}_{pj}\right)}{\mathrm{d}\tau}+2\zeta_{pb2}\dfrac{\mathrm{d}\overline{x}_{pb2}}{\mathrm{d}\tau}=-f_{pb2x}\\ \dfrac{\mathrm{d}^2\overline{y}_{pb2}}{\mathrm{d}\tau^2}+k_{ppb2y}\left(2\overline{y}_{pb2}-\overline{y}^{\mathrm{I}}_{pj}-\overline{y}^{\mathrm{II}}_{pj}\right)+2\zeta_{ppb2y}\dfrac{\mathrm{d}\left(2\overline{y}_{pb2}-\overline{y}^{\mathrm{I}}_{pj}-\overline{y}^{\mathrm{II}}_{pj}\right)}{\mathrm{d}\tau}+2\zeta_{pb2}\dfrac{\mathrm{d}\overline{y}_{pb2}}{\mathrm{d}\tau}=-f_{pb2y}-f_g\\ \dfrac{\mathrm{d}^2\overline{z}_{pb2}}{\mathrm{d}\tau^2}+k_{ppb2z}\left(2\overline{z}_{pb2}-\overline{z}^{\mathrm{I}}_{pj}-\overline{z}^{\mathrm{II}}_{pj}\right)+2\zeta_{ppb2z}\dfrac{\mathrm{d}\left(2\overline{z}_{pb2}-\overline{z}^{\mathrm{I}}_{pj}-\overline{z}^{\mathrm{II}}_{pj}\right)}{\mathrm{d}\tau}+2\zeta_{pb2}\dfrac{\mathrm{d}\overline{z}_{pb2}}{\mathrm{d}\tau}=-f_{pb2z}\end{cases}\tag{54}$$

External meshing planetary gear:

$$\begin{cases}\dfrac{\mathrm{d}^2\overline{u}^{\mathrm{II}}_{pj}}{\mathrm{d}\tau^2}+k^{\mathrm{II}}_{up}\left(\overline{u}^{\mathrm{II}}_{pj}-\overline{u}^{\mathrm{I}}_{pj}\dfrac{r^{\mathrm{II}}_{bp}}{r^{\mathrm{I}}_{bp}}\right)+2\zeta^{\mathrm{II}}_{up}\dfrac{\mathrm{d}\left(\overline{u}^{\mathrm{II}}_{pj}-\overline{u}^{\mathrm{I}}_{pj}r^{\mathrm{II}}_{bp}/r^{\mathrm{I}}_{bp}\right)}{\mathrm{d}\tau}+\left(\vec{f}^{\mathrm{II}}_{mjpj}\vec{r}^{\mathrm{II}}_{bp}-\overline{M}^{\mathrm{II}}_{pj}\right)\cos\beta^{\mathrm{II}}=0\\ \dfrac{\mathrm{d}^2\overline{x}^{\mathrm{II}}_{pj}}{\mathrm{d}\tau^2}+k^{\mathrm{II}}_{ppjx}\left(\overline{x}^{\mathrm{II}}_{pj}-\overline{x}_{pb2}\right)+2\zeta^{\mathrm{II}}_{ppjx}\dfrac{\mathrm{d}\left(\overline{x}^{\mathrm{II}}_{pj}-\overline{x}_{pb2}\right)}{\mathrm{d}\tau}-\left(f^{\mathrm{II}}_{mjpj}\sin\psi^{\mathrm{II}}_j-f^{\mathrm{II}}_{fpj}\cos\psi^{\mathrm{II}}_j\right)=0\\ \dfrac{\mathrm{d}^2\overline{y}^{\mathrm{II}}_{pj}}{\mathrm{d}\tau^2}+k^{\mathrm{II}}_{ppjy}\left(\overline{y}^{\mathrm{II}}_{pj}-\overline{y}_{pb2}\right)+2\zeta^{\mathrm{II}}_{ppjy}\dfrac{\mathrm{d}\left(\overline{y}^{\mathrm{II}}_{pj}-\overline{y}_{pb2}\right)}{\mathrm{d}\tau}-\left(f^{\mathrm{II}}_{mjpj}\cos\psi^{\mathrm{II}}_j-f^{\mathrm{II}}_{fpj}\sin\psi^{\mathrm{II}}_j\right)\cos\beta^{\mathrm{II}}=0\\ \dfrac{\mathrm{d}^2\overline{z}^{\mathrm{II}}_{pj}}{\mathrm{d}\tau^2}+k^{\mathrm{II}}_{ppjz}\left(\overline{z}^{\mathrm{II}}_{pj}-\overline{z}_{pb2}\right)+2\zeta^{\mathrm{II}}_{ppjz}\dfrac{\mathrm{d}\left(\overline{z}^{\mathrm{I}}_{pj}-\overline{z}_{pb2}\right)}{\mathrm{d}\tau}+\left(f^{\mathrm{II}}_{mjpj}\cos\psi^{\mathrm{II}}_j-f^{\mathrm{II}}_{fpj}\sin\psi^{\mathrm{II}}_j\right)\sin\beta^{\mathrm{II}}=0\end{cases}\tag{55}$$

Sun gear bearing 1:

$$\begin{cases}\dfrac{\mathrm{d}^2\overline{x}_{sb}}{\mathrm{d}\tau^2}+k_{ssbx}(\overline{x}_{sb}-\overline{x}_s)+2\zeta_{ssbx}\dfrac{\mathrm{d}(\overline{x}_{sb}-\overline{x}_s)}{\mathrm{d}\tau}+2\zeta_{sb}\dfrac{\mathrm{d}\overline{x}_{sb}}{\mathrm{d}\tau}=-f_{sbx}\\ \dfrac{\mathrm{d}^2\overline{y}_{sb}}{\mathrm{d}\tau^2}+k_{ssby}(\overline{y}_{sb}-\overline{y}_s)+2\zeta_{ssby}\dfrac{\mathrm{d}(\overline{y}_{sb}-\overline{y}_s)}{\mathrm{d}\tau}+2\zeta_{sb}\dfrac{\mathrm{d}\overline{y}_{sb}}{\mathrm{d}\tau}=-f_{sby}-f_g\\ \dfrac{\mathrm{d}^2\overline{z}_{sb}}{\mathrm{d}\tau^2}+k_{ssbz}(\overline{z}_{sb}-\overline{z}_s)+2\zeta_{ssbz}\dfrac{\mathrm{d}(\overline{z}_{sb}-\overline{z}_s)}{\mathrm{d}\tau}+2\zeta_{sb}\dfrac{\mathrm{d}\overline{z}_{sb}}{\mathrm{d}\tau}=-f_{sbz}\end{cases}\tag{56}$$

Sun gear:

$$\begin{cases}\dfrac{\mathrm{d}^2\overline{u}_s}{\mathrm{d}\tau^2}+k_{us}\left(\overline{u}_s-\overline{u}_1\dfrac{r_{bs}}{r_1}\right)+2\zeta_{us}\dfrac{\mathrm{d}(\overline{u}_s-\overline{u}_1r_{bs}/r_1)}{\mathrm{d}\tau}-\sum\limits_{j=1}^{3}\left(\vec{f}^{\mathrm{II}}_{mjs}\vec{r}_{bs}-\overline{M}_s\right)\cos\beta^{\mathrm{II}}=0\\ \dfrac{\mathrm{d}^2\overline{x}_s}{\mathrm{d}\tau^2}+k_{ssx}(2\overline{x}_s-\overline{x}_1-\overline{x}_{sb})+2\zeta_{ssx}\dfrac{\mathrm{d}(2\overline{x}_s-\overline{x}_1-\overline{x}_{sb})}{\mathrm{d}\tau}+\sum\limits_{j=1}^{3}\left(f^{\mathrm{II}}_{mjs}\sin\psi^{\mathrm{II}}_j-f^{\mathrm{II}}_{fs}\cos\psi^{\mathrm{II}}_j\right)=0\\ \dfrac{\mathrm{d}^2\overline{y}_s}{\mathrm{d}\tau^2}+k_{ssy}(2\overline{y}_s-\overline{y}_1-\overline{y}_{sb})+2\zeta_{ssy}\dfrac{\mathrm{d}(2\overline{y}_s-\overline{y}_1-\overline{y}_{sb})}{\mathrm{d}\tau}+\sum\limits_{j=1}^{3}\left(f^{\mathrm{II}}_{mjs}\cos\psi^{\mathrm{II}}_j-f^{\mathrm{II}}_{fs}\sin\psi^{\mathrm{II}}_j\right)\cos\beta^{\mathrm{II}}=-f_g\\ \dfrac{\mathrm{d}^2\overline{z}_s}{\mathrm{d}\tau^2}+k_{ssz}(2\overline{z}_s-\overline{z}_1-\overline{z}_{sb})+2\zeta_{ssz}\dfrac{\mathrm{d}(2\overline{z}_s-\overline{z}_1-\overline{z}_{sb})}{\mathrm{d}\tau}-\sum\limits_{j=1}^{3}\left(f^{\mathrm{II}}_{mjs}\cos\psi^{\mathrm{II}}_j-f^{\mathrm{II}}_{fs}\sin\psi^{\mathrm{II}}_j\right)\sin\beta^{\mathrm{II}}=0\end{cases}\tag{57}$$

Herringbone Gear 1:

$$\begin{cases}\dfrac{\mathrm{d}^2\overline{u}_1}{\mathrm{d}\tau^2}+k_{u1}\left(\overline{u}_1-\overline{u}_s\dfrac{r_{b1}}{r_{bs}}\right)+2\zeta_{u1}\dfrac{\mathrm{d}\left(\overline{u}_1-\overline{u}_s\dfrac{r_{b1}}{r_{bs}}\right)}{\mathrm{d}\tau}+\left(f^{\mathrm{III}}_{m1}r_{b1}-\overline{M}_1\right)\cos\beta^{\mathrm{III}}=0\\ \dfrac{\mathrm{d}^2\overline{x}_1}{\mathrm{d}\tau^2}+k_{s1x}(2\overline{x}_1-\overline{x}_s-\overline{x}_{1b})+2\zeta_{s1x}\dfrac{\mathrm{d}(2\overline{x}_1-\overline{x}_s-\overline{x}_{1b})}{\mathrm{d}\tau}-\left(f^{\mathrm{III}}_{m1}\sin\alpha^{\mathrm{III}}_n-f^{\mathrm{III}}_{f1}\cos\alpha^{\mathrm{III}}_n\right)=0\\ \dfrac{\mathrm{d}^2\overline{y}_1}{\mathrm{d}\tau^2}+k_{s1y}(2\overline{y}_1-\overline{y}_s-\overline{y}_{1b})+2\zeta_{s1y}\dfrac{\mathrm{d}(2\overline{y}_1-\overline{y}_s-\overline{y}_{1b})}{\mathrm{d}\tau}+\left(f^{\mathrm{III}}_{m1}\cos\alpha^{\mathrm{III}}_n-f^{\mathrm{III}}_{f1}\sin\alpha^{\mathrm{III}}_n\right)\cos\beta^{\mathrm{III}}=-f_g\\ \dfrac{\mathrm{d}^2\overline{z}_1}{\mathrm{d}\tau^2}+k_{s1z}(2\overline{z}_1-\overline{z}_s-\overline{z}_{1b})+2\zeta_{s1z}\dfrac{\mathrm{d}(2\overline{z}_1-\overline{z}_s-\overline{z}_{1b})}{\mathrm{d}\tau}=0\end{cases}\tag{58}$$

Herringbone gear bearing 1:

$$\begin{cases}\dfrac{\mathrm{d}^2\overline{x}_{1b}}{\mathrm{d}\tau^2}+k_{s1bx}(\overline{x}_{1b}-\overline{x}_1)+2\zeta_{s1bx}\dfrac{\mathrm{d}(\overline{x}_{1b}-\overline{x}_1)}{\mathrm{d}\tau}+2\zeta_{1b}\dfrac{\mathrm{d}\overline{x}_{1b}}{\mathrm{d}\tau}=-f_{1bx}\\ \dfrac{\mathrm{d}^2\overline{y}_{1b}}{\mathrm{d}\tau^2}+k_{s1by}(\overline{y}_{1b}-\overline{y}_1)+2\zeta_{s1by}\dfrac{\mathrm{d}(\overline{y}_{1b}-\overline{y}_1)}{\mathrm{d}\tau}+2\zeta_{1b}\dfrac{\mathrm{d}\overline{y}_{1b}}{\mathrm{d}\tau}=-f_{1by}-f_g\\ \dfrac{\mathrm{d}^2\overline{z}_{1b}}{\mathrm{d}\tau^2}+k_{s1bz}(\overline{z}_{1b}-\overline{z}_1)+2\zeta_{s1bz}\dfrac{\mathrm{d}(\overline{z}_{1b}-\overline{z}_1)}{\mathrm{d}\tau}+2\zeta_{1b}\dfrac{\mathrm{d}\overline{z}_{1b}}{\mathrm{d}\tau}=-f_{1bz}\end{cases}\tag{59}$$

Herringbone Gear 2:

$$\begin{cases}\dfrac{\mathrm{d}^2\overline{u}_2}{\mathrm{d}\tau^2}+k_{u2}\overline{u}_2+2\zeta_{u2}\dfrac{\mathrm{d}\overline{u}_2}{\mathrm{d}\tau}-\left(f^{\mathrm{III}}_{m2}r_{b2}-\overline{M}_2\right)\cos\beta^{\mathrm{III}}=t_{\mathrm{out}}\\ \dfrac{\mathrm{d}^2\overline{x}_2}{\mathrm{d}\tau^2}+k_{22x}(2\overline{x}_2-\overline{x}_{21b}-\overline{x}_{22b})+2\zeta_{22x}\dfrac{\mathrm{d}(2\overline{x}_2-\overline{x}_{21b}-\overline{x}_{22b})}{\mathrm{d}\tau}+\left(f^{\mathrm{III}}_{m2}\sin\alpha^{\mathrm{III}}_n-f^{\mathrm{III}}_{f2}\cos\alpha^{\mathrm{III}}_n\right)=-f_g\\ \dfrac{\mathrm{d}^2\overline{y}_2}{\mathrm{d}\tau^2}+k_{22y}(2\overline{y}_2-\overline{y}_{21b}-\overline{y}_{22b})+2\zeta_{22y}\dfrac{\mathrm{d}(2\overline{y}_2-\overline{y}_{21b}-\overline{y}_{22b})}{\mathrm{d}\tau}-\left(f^{\mathrm{III}}_{m2}\cos\alpha^{\mathrm{III}}_n-f^{\mathrm{III}}_{f2}\sin\alpha^{\mathrm{III}}_n\right)\cos\beta^{\mathrm{III}}=0\end{cases}\tag{60}$$

Herringbone gear bearing 21:

$$\begin{cases}\dfrac{\mathrm{d}^2\overline{x}_{21b}}{\mathrm{d}\tau^2}+k_{221x}(\overline{x}_{21b}-\overline{x}_2)+2\zeta_{221x}\dfrac{\mathrm{d}(2\overline{x}_{21b}-\overline{x}_2)}{\mathrm{d}\tau}+2\zeta_{21b}\dfrac{\mathrm{d}\overline{x}_{21b}}{\mathrm{d}\tau}=-f_{21bx}\\ \dfrac{\mathrm{d}^2\overline{y}_{21b}}{\mathrm{d}\tau^2}+k_{221y}(2\overline{y}_{21b}-\overline{y}_2)+2\zeta_{221y}\dfrac{\mathrm{d}(2\overline{y}_{21b}-\overline{y}_2)}{\mathrm{d}\tau}+2\zeta_{21b}\dfrac{\mathrm{d}\overline{y}_{21b}}{\mathrm{d}\tau}=-f_{21by}-f_g\end{cases}\tag{61}$$

Herringbone gear bearing 22:

$$\begin{cases}\dfrac{\mathrm{d}^2\overline{x}_{22b}}{\mathrm{d}\tau^2}+k_{222bx}(\overline{x}_{22b}-\overline{x}_{21})+2\zeta_{222bx}\dfrac{\mathrm{d}(\overline{x}_{22b}-\overline{x}_{21})}{\mathrm{d}\tau}+2\zeta_{22b}\dfrac{\mathrm{d}\overline{x}_{22b}}{\mathrm{d}\tau}=-f_{22bx}\\ \dfrac{\mathrm{d}^2\overline{y}_{22b}}{\mathrm{d}\tau^2}+k_{222by}(\overline{y}_{22b}-\overline{y}_{21})+2\zeta_{222by}\dfrac{\mathrm{d}(\overline{y}_{22b}-\overline{y}_{21})}{\mathrm{d}\tau}+2\zeta_{22b}\dfrac{\mathrm{d}\overline{y}_{22b}}{\mathrm{d}\tau}=-f_{22by}-f_g\end{cases}\tag{62}$$

where: $\overline{u}_q=\dfrac{u_q}{b^{\mathrm{II}}}$, $\overline{x}_q=\dfrac{x_q}{b^{\mathrm{II}}}$, $\overline{y}_i=\dfrac{y_q}{b^{\mathrm{II}}}$, $\overline{z}_i=\frac{z_q}{b^{\mathrm{II}}}$, $\tau=\omega_n t$, $\zeta_{pqh}=\dfrac{C_{pqh}}{2m_q\omega_n}$, $\zeta_{sqh}=\dfrac{C_{sqh}}{2m_q\omega_n}$, $\zeta_{2qh}=\dfrac{C_{2qh}}{2m_q\omega_n}$, $k^k_{pqh}=\dfrac{K_{pqh}}{m^k_q\omega^2_n}$, $k_{sqj}=\dfrac{K_{sqh}}{m_q\omega^2_n}$, $k_{2qh}=\dfrac{K_{2qh}}{m_q\omega^2_n}$, $k_e=\dfrac{K_e}{(I_{ri}/r^2_{br})\omega^2_n}$, $f_g=\dfrac{g}{b^{\mathrm{II}}\omega^2_n}$, $f^k_{mq}=\dfrac{F^k_{mq}}{m^k_qb^{\mathrm{II}}\omega^2_n}$, $f^k_{fq}=\dfrac{F^k_{fq}}{m^k_qb^{\mathrm{II}}\omega^2_n}$, $\psi^k_j=\alpha^k_n+\varphi^k_j$, $t_u=\dfrac{T_u}{(I_{ri}/r^2_{br})\omega^2_n(b^{\mathrm{II}})^2}$, $\overline{f}^{\mathrm{I}}_{mjr}=\dfrac{F^{\mathrm{I}}_{mjr}}{(I_{ri}/r^2_{br})b^{\mathrm{II}}\omega^2_n}$, $\overline{M}_{ri}=\dfrac{M_{ri}}{(I_{ri}/r^2_{br})\omega^2_n(b^{\mathrm{II}})^2}$, $\overline{M}^k_q=\frac{M^k_q}{m^k_q}$ $\quad\omega^2_n(b^{\mathrm{II}})^2\lambda_i=\xi+\varphi_{ri}+u_{ri};\eta_i=\xi-\varphi_{ri-1}-u_{ri}$ $(q=r,pj,s,1,2,pb1,pb2,sb,1b,\ 21b,22b;h=x,y,z;k=\mathrm{I},\mathrm{II},\mathrm{III};u=in,out)$.

Tables 2 and 3 display the gear and bearing specifications used in this article.

4 System dynamic response

In this part, the impact of external load excitation frequency on the system's dynamic properties is examined. The fourth-order Runge–Kutta method is used to solve Eqs. (36)–(62), and the initial displacement and initial velocity of the system are set 0, a minute later, the vibration displacement response of NW wind power transmission system is obtained. The Poincaré section method is used to solve the system bifurcation diagram, and the excitation is traversed. The excitation frequency or meshing stiffness is used to record the vibration of the system in a stable state. In terms of dynamic displacement, the relationship between vibration displacement and parameters is drawn. The corresponding bifurcation diagram is obtained.

Figures 13, 14, and 15 examine how the equivalent displacement $\overline{x}_{n1}, \overline{x}_{n2}, \overline{x}_{n3}$ has changed along the system's three meshing lines when the excitation frequency ω_e is 0.170, 0.205, and 0.245. When $\omega_e = 0.170$, The time history of the equivalent displacement $\overline{x}_{n1}$ shows oscillatory motion with a periodicity of 2 T, and in the FFT spectrum, the dominant frequency component is the meshing frequency f_{m}, followed by the secondary presence of the double meshing frequency $2 f_{\mathrm{m}}$; the phase diagram displays a closed annulus with two windings. There are just two dots on the Poincaré map, showing that the low-speed gear pair is roughly conforming to the period-doubling motion. The time history of the equivalent displacement $\overline{x}_{n2}$ exhibits periodic oscillatory motion, and in the FFT spectrum, the dominant frequency component is the meshing frequency f_{m}, followed by the secondary presence of the double meshing frequency as well as the triple meshing frequency. The phase diagram displays a closed circle, with just one dot on the Poincaré map, indicating that the intermediate gear pair is in periodic motion. The time history of the equivalent displacement $\overline{x}_{n3}$ displays chaotic oscillatory motion, and in the FFT spectrum, the dominant frequency component is the meshing frequency f_{m}, accompanied by a broad-spectrum presence; the phase diagram forms a closed annulus with many windings, and the Poincaré map displays chaotic disordered dots, indicating that the high-speed gear is in chaotic motion.

When $\omega_e = 0.205$, the time history of the equivalent displacement $\overline{x}_{n1}$ displays chaotic oscillatory motion, and in the FFT spectrum, the dominant frequency component is the meshing frequency f_{m}, accompanied by a broad-spectrum presence. The phase diagram forms a closed annulus with many windings, and the Poincaré map displays chaotic disordered dots, showing that the low-speed gear pair is in chaotic motion. The time history of the equivalent displacement $\overline{x}_{n2}$ displays chaotic oscillatory motion, and in the FFT spectrum, the dominant frequency component is the meshing frequency f_{m}, accompanied by a broad-spectrum presence. The phase diagram of the equivalent displacement $\overline{x}_{n2}$ of the intermediate gear pair is a closed annulus with many windings, and the Poincaré map displays chaotic disordered dots, showing that the intermediate gear pair is in chaotic motion. The time history of the equivalent displacement $\overline{x}_{n3}$ shows periodic oscillatory motion, and in the FFT spectrum, the dominant frequency component is one-third of the meshing frequency $1/3\, f_{\mathrm{m}}$, accompanied by a broad-spectrum presence. The phase diagram displays a closed annulus with one winding, and there are three dots on the Poincaré map, showing that the high-speed gear pair is roughly conforming to the period-doubling motion.

Table 2 Gear parameters of NW wind power speed increaser

Parameters	r	p_{1j}	p_{2j}	s	h_1	h_2
Tooth numbers Z	91	22	83	40	131	20
Modules m_n (mm)	28	16	10			
Pressure angle α (°)	20	20	15			
Helix angle β (°)	4.0	7.2	32.0			
Gear width B (mm)	560	410	365			
Gear backlash b (mm)	45	55	50			
Gear quality M (kg)	5690	950	2320	440	5369	125
Backlash $2b_m$ (μm)	110	100	90	90	100	100

When $\omega_e = 0.245$, the time history of the equivalent displacement $\overline{x}_{n1}$ shows oscillatory motion with a periodicity of 2 T, and in the FFT spectrum, the dominant frequency component is the meshing frequency f_{m}; the phase diagram of the equivalent

Table 3 Basic parameters of the bearing

Parameters	$pb1$	$pb2$	sb	$1b$	$21b$	$22b$
Number of rollers Z_b	16	11	12	13	12	12
Inner diameter r_{bi} (mm)	160	300	100	350	40	40
Outer diameter r_{bo} (mm)	240	365	180	465	70	70
Mass M_b (kg)	47	121	50	295	2.2	2.2
Bearing clearance c_b (μm)	180	160	55	305	50	50
Support stiffness K_b (N/m)	5×10^9	8×10^9	8×10^9	5×10^9	8×10^9	2×10^9

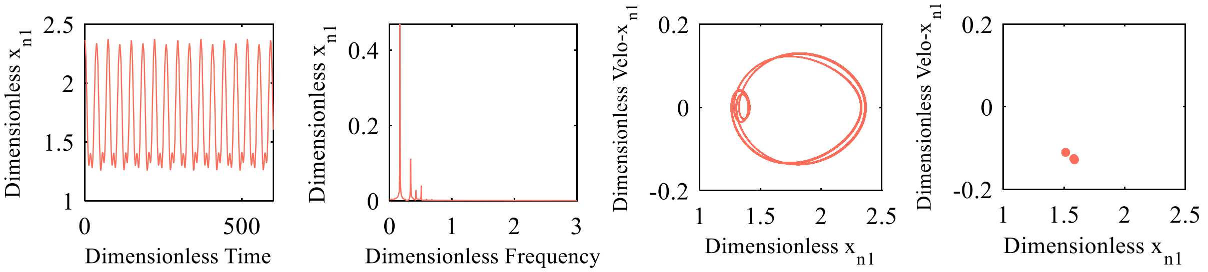

(a1) Time history (b1) FFT spectrum (c1) Phase diagram (d1) Poincaré map

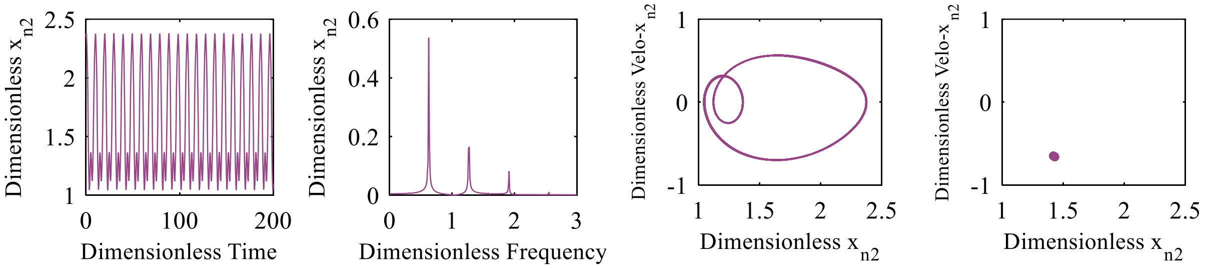

(a2) Time history (b2) FFT spectrum (c2) Phase diagram (d2) Poincaré map

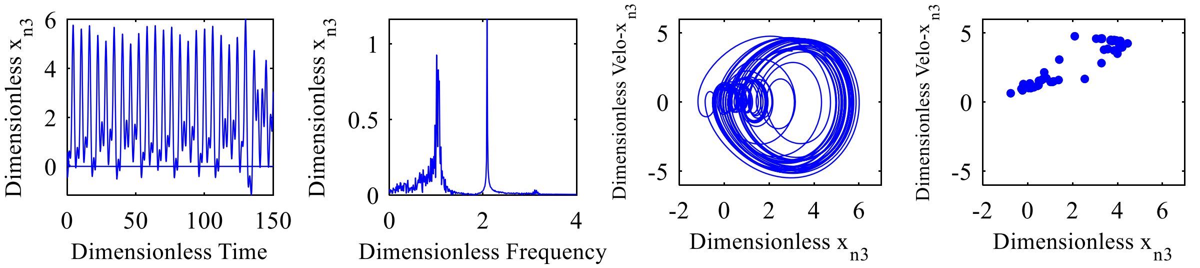

(a3) Time history (b3) FFT spectrum (c3) Phase diagram (d3) Poincaré map

(1) Low-speed gear pair (2) Intermediate gear pair (3) High-speed gear

Fig. 13 Meshing displacement vibration response when ω_{e} = 0.170. (a1) Time history, (b1) FFT spectrum, (c1) Phase diagram, (d1) Poincaré map. (a2) Time history, (b2) FFT spectrum, (c2) Phase diagram, (d2) Poincaré map. (a3) Time history, (b3) FFT spectrum, (c3) Phase diagram, (d3) Poincaré map. (1) Low-speed gear pair (2) Intermediate gear pair (3) High-speed gear

displacement $\bar{x}_{n1}$ of the low-speed gear pair forms a closed annulus with two windings, and there are just two dots on the Poincaré map, showing that the low-speed gear pair is roughly conforming to the period-doubling motion. The time history of the equivalent displacement $\bar{x}_{n2}$ shows oscillatory motion with a periodicity of 2 T, and in the FFT spectrum, the dominant frequency component is the meshing frequency f_{m}; the phase diagram of the equivalent displacement $\bar{x}_{n2}$ of the intermediate gear pair is a closed annulus with two windings, and there are just two dots on the Poincaré map, showing that the intermediate gear pair is roughly conforming to the period-doubling motion. The time history of the equivalent displacement $\bar{x}_{n3}$ exhibits chaotic oscillatory motion, and in the FFT spectrum, there is only one meshing frequency f_{m} present; the phase diagram displays a closed annulus with many windings, and the Poincaré map displays chaotic disordered dots, showing that the high-speed gear pair is in chaotic motion.

The phase trajectory plane and 3D frequency spectrum of the gear pair are depicted in Figs. 16 and 17. It can be inferred from the phase trajectory plane and the 3D frequency spectrum that the three-stage gear pair will transition between periodic motion state, double-periodic motion state, and chaotic motion state with a change in excitation frequency.

Wavelet analysis is established to determine time–frequency characteristics of the three-stage gear pair,

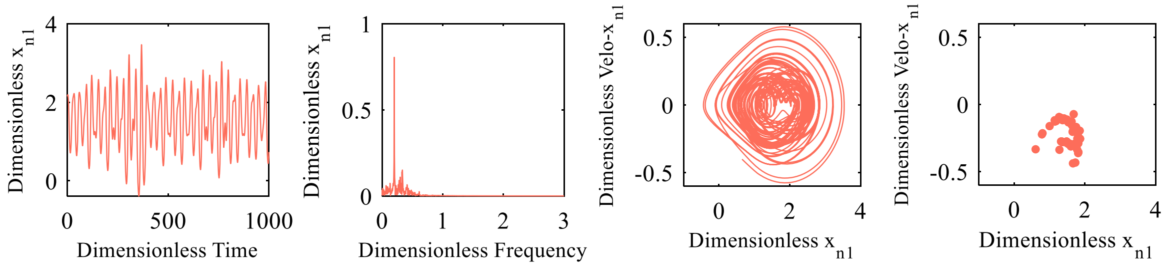

(a1) Time history (b1) FFT spectrum (c1) Phase diagram (d1) Poincaré map

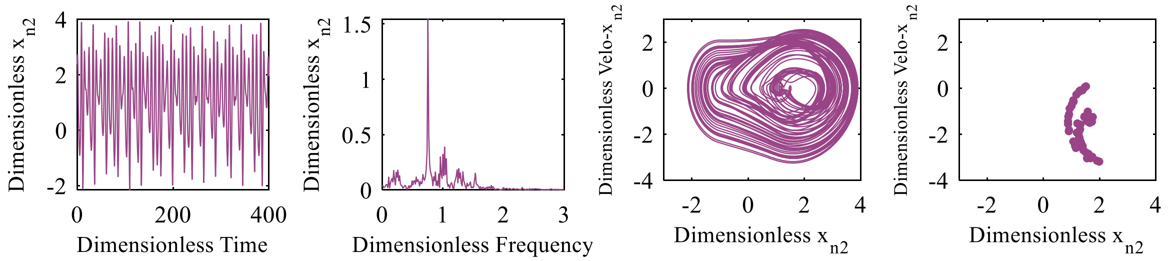

(a2) Time history (b2) FFT spectrum (c2) Phase diagram (d2) Poincaré map

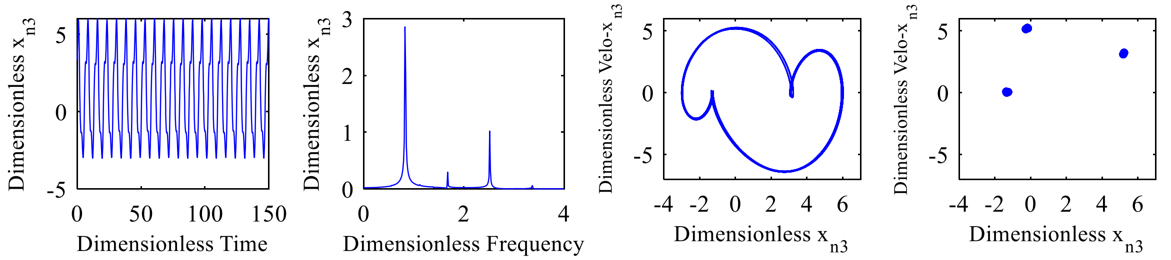

(a3) Time history (b3) FFT spectrum (c3) Phase diagram (d3) Poincaré map

(1) Low-speed gear pair (2) Intermediate gear pair (3) High-speed gear

Fig. 14 Meshing displacement vibration response when ω_{e} = 0.205. (a1) Time history, (b1) FFT spectrum, (c1) Phase diagram, (d1) Poincaré map. (a2) Time history, (b2) FFT spectrum, (c2) Phase diagram, (d2) Poincaré map. (a3) Time history, (b3) FFT spectrum, (c3) Phase diagram, (d3) Poincaré map. (1) Low-speed gear pair (2) Intermediate gear pair (3) High-speed gear

which are displayed in Fig. 18. When the system transitions into a state of a periodic or double-periodic motion, only one or more frequencies will appear in the time–frequency diagram. When the gear pair transitions into a state of chaotic motion, a certain width of the discrete frequency spectrum will appear in the time–frequency diagram.

The bifurcation diagram with ω_e as the bifurcation parameter is drawn using the fourth-order Runge–Kutta integration with varying steps to better highlight the impact of excitation frequency on the dynamic properties of the system. Figures 19, 20, and 21 depict diagrams of the three-stage gear pairs. When ω_e is smaller than 0.204, Fig. 19 demonstrates that the equivalent displacement $\bar{x}_{n1}$ executes periodic motion. The equivalent displacement performs chaotic motion when $\omega_e \in (0.204, 0.212)$. When $\omega_e \in (0.212, 0.220)$, the equivalent displacement from the chaotic condition to perform period-doubling motion. The equivalent displacement returns to a chaotic state when $\omega_e > 0.220$. When $\omega_e \in (0.245, 0.260)$, the equivalent displacement eliminates the chaotic condition, performs period-doubling motion, and then executes periodic motion when $\omega_e > 0.260$.

Figure 20 demonstrates that the equivalent displacement $\bar{x}_{n2}$ executes periodic motion when $\omega_e \in (0.160, 0.187)$. When $\omega_e \in (0.187, 0.218)$, the equivalent displacement exhibits chaotic motion. The equivalent displacement eliminates the chaotic condition and exhibits period-doubling motion when

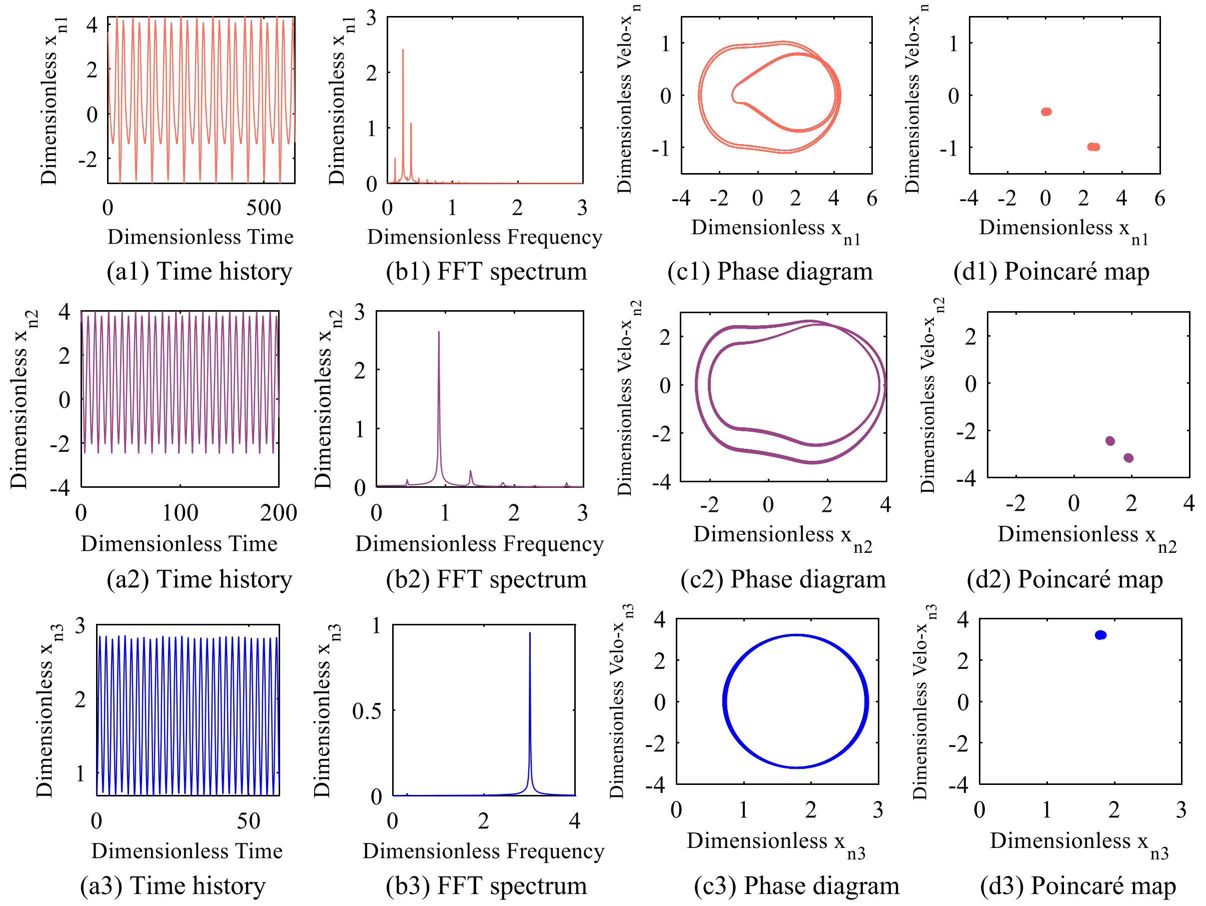

(a1) Time history (b1) FFT spectrum (c1) Phase diagram (d1) Poincaré map

(a2) Time history (b2) FFT spectrum (c2) Phase diagram (d2) Poincaré map

(a3) Time history (b3) FFT spectrum (c3) Phase diagram (d3) Poincaré map

(1) Low-speed gear pair (2) Intermediate gear pair (3) High-speed gear

Fig. 15 Meshing displacement vibration response when ω_{e} = 0.245. (a1) Time history, (b1) FFT spectrum, (c1) Phase diagram, (d1) Poincaré map. (a2) Time history, (b2) FFT spectrum, (c2) Phase diagram, (d2) Poincaré map. (a3) Time history, (b3) FFT spectrum, (c3) Phase diagram, (d3) Poincaré map. (1) Low-speed gear pair (2) Intermediate gear pair (3) High-speed gear

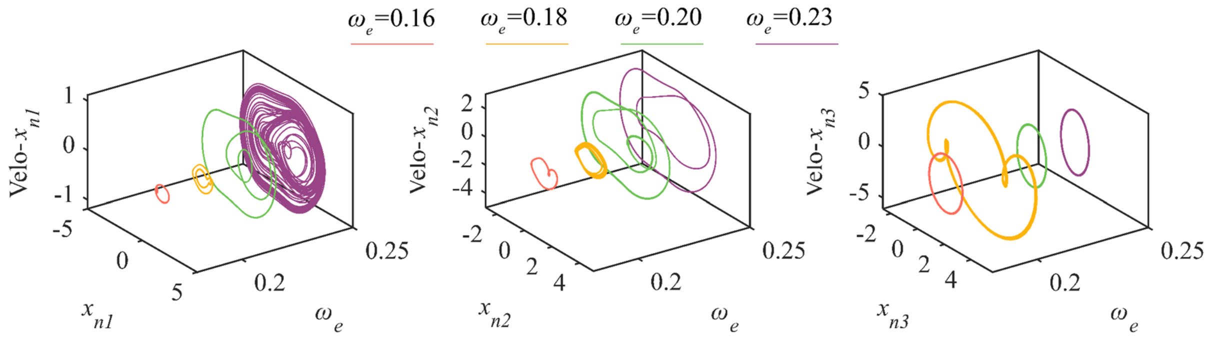

(a) Low-speed gear pair (b) Intermediate gear pair (c) High-speed gear pair

Fig. 16 Phase trajectory plane. **a** Low-speed gear pair, **b** Intermediate gear pair, **c** High-speed gear pair

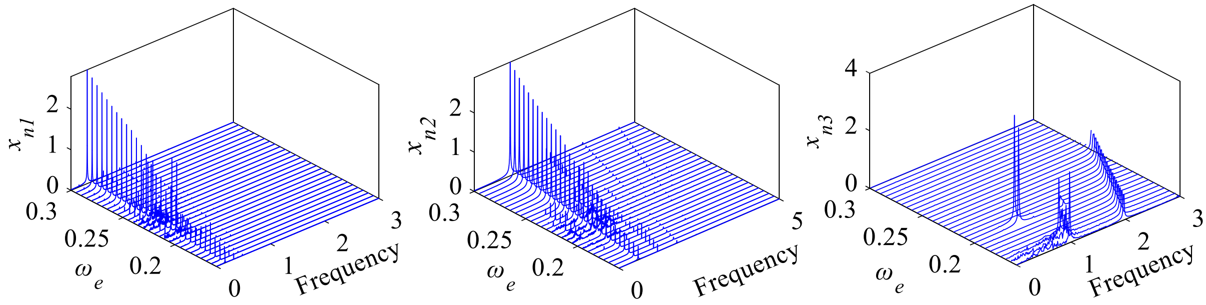

(a) Low-speed gear pair (b) Intermediate gear pair (c) High-speed gear pair

Fig. 17 3D frequency spectrum. **a** Low-speed gear pair, **b** Intermediate gear pair, **c** High-speed gear pair

$\omega_e > 0.218$. When $\omega_e > 0.223$, the equivalent displacement returns to a chaotic state. Furthermore, when ω_e is > 0.236, the equivalent displacement from the chaotic condition to period-doubling motion and then executes periodic motion when $\omega_e > 0.246$.

Figure 21 demonstrates that the equivalent displacement $\bar{x}_{n3}$ executes chaos motion when $\omega_e \in (0.160, 0.175)$. The equivalent displacement transitions from the chaotic condition to period-doubling motion when $\omega_e \in (0.175, 0.180)$. Subsequently, when $\omega_e \in (0.180, 0.196)$, the equivalent displacement exits the period-doubling motion state and enters the periodic motion state. When $\omega_e > 0.196$, the high-speed gear pair's equivalent displacement $\bar{x}_{n3}$ executes period-doubling motion until $\omega_e > 0.210$, at which point it transitions to periodic motion.

5 Super harmonic resonance characteristics analysis of NW planetary gear system

5.1 Multiple-scales analysis of the NW planetary gear system

If just torsional vibration is taken into account, the relative equivalent displacement vibration equation of the three-stage gear pair can be simplified as follows.

(1) Low-speed gear pair with time delay:

$$\frac{d^2\bar{x}_n^{\mathrm{I}}}{d\tau^2} + 3\left[2\zeta_{m1}\frac{d\bar{x}_n^{\mathrm{I}}}{d\tau} + (k_{m1} + k_{m1}k\cos(\omega_{m1}\tau))f(\bar{x}_n^{\mathrm{I}})\right] \cos\alpha_n^{\mathrm{I}}\cos\beta^{\mathrm{I}} = f_0^{\mathrm{I}} + f_1\cos(v_1\tau) + g_{d1}\bar{x}_n^{\mathrm{I}}(\tau - \tau_d) + g_{v1}\frac{d\bar{x}_n^{\mathrm{I}}}{d\tau}(\tau - \tau_d) \tag{63}$$

(2) Intermediate gear pair with time delay:

$$\frac{d^2\bar{x}_n^{\mathrm{II}}}{d\tau^2} + 3\left[2\zeta_{m2}\frac{d\bar{x}_n^{\mathrm{II}}}{d\tau} + (1 + k\cos(\omega_{m1}\tau))f(\bar{x}_n^{\mathrm{II}})\right] \cos\alpha_n^{\mathrm{II}}\cos\beta^{\mathrm{II}} = f_0^{\mathrm{II}} + f_2\cos(v_2\tau) + g_{d1}\bar{x}_n^{\mathrm{II}}(\tau - \tau_d) + g_{v2}\frac{d\bar{x}_n^{\mathrm{II}}}{d\tau}(\tau - \tau_d) \tag{64}$$

(3) High-speed gear pair with time delay:

$$\frac{d^2\bar{x}_n^{\mathrm{III}}}{d\tau^2} + \left[2\zeta_{m3}\frac{d\bar{x}_n^{\mathrm{III}}}{d\tau} + k_{m3}(1 + k\cos(\omega_{m3}\tau))f(\bar{x}_n^{\mathrm{III}})\right] \cos\alpha_n^{\mathrm{III}}\cos\beta^{\mathrm{III}} = f_0^{\mathrm{III}} + f_3\cos(v_3\tau) + \left(g_{d3}\bar{x}_n^{\mathrm{III}} + g_{v3}\frac{d\bar{x}_n^{\mathrm{III}}}{d\tau}\right)(\tau - \tau_d) \tag{65}$$

where f_0^k is the dimensionless external excitation force equivalent static load, f^k is the dimensionless external excitation force fluctuation amplitude, k_{mi} is dimensionless meshing stiffness, ζ_{mi} is dimensionless meshing damping, the displacement delay $\bar{x}_n^{\mathrm{III}}(\tau - \tau_d)$ represents the time difference of the equivalent

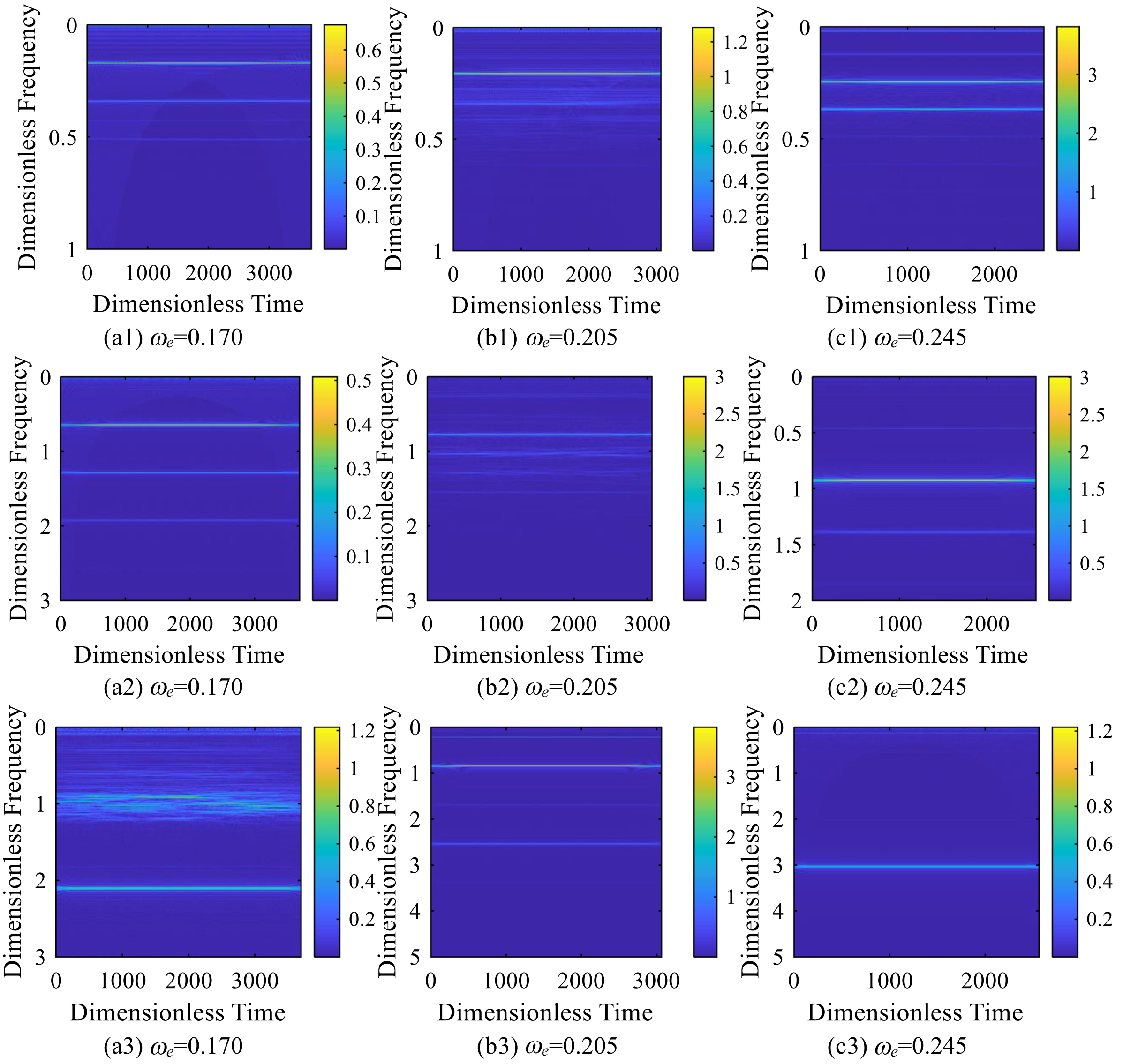

(a1) ω_e=0.170 (b1) ω_e=0.205 (c1) ω_e=0.245

(a2) ω_e=0.170 (b2) ω_e=0.205 (c2) ω_e=0.245

(a3) ω_e=0.170 (b3) ω_e=0.205 (c3) ω_e=0.245

(1) Low-speed gear pair (2) Intermediate gear pair (3) High-speed gear

Fig. 18 Time–frequency. (a1) ω_e = 0.170, (b1) ω_e = 0.205, (c1) ω_e = 0.245. (a2) ω_e = 0.170, (b2) ω_e = 0.205, (c2) ω_e = 0.245. (a3) ω_e = 0.170, (b3) ω_e = 0.205, (c3) ω_e = 0.245. (1) Low-speed gear pair (2) Intermediate gear pair (3) High-speed gear

displacement x_n before and after the active control is applied, and the corresponding displacement control parameters is g_{di}; the velocity delay $\mathrm{d}\overline{x}_n^{\mathrm{III}}/\mathrm{d}\tau(\tau - \tau_d)$ represents the time difference of the relative velocity $\dot{x}_n$ on the meshing line before and after the active control is applied, and the corresponding speed control parameters is g_{vi}. (k = I, II, III; i = 1, 2, 3).

The third-order polynomial, which is fitted to the tooth-backlash function $f(\overline{x}_n)$, may properly depict the meshing of the system.

$$f(\overline{x}_n) = \delta_1\overline{x}_n + \delta_2\overline{x}_n^3 = \delta_1(\overline{x}_n + \delta_0\overline{x}_n^3) \tag{66}$$

Introduce a high-level minim ε, $|\varepsilon| < < 1$, and specify time variables for various scales.

$$T_i = \varepsilon^i \, (i = 0, 1, 2\ldots) \tag{67}$$

The vibration displacement is described as a function of time variables with various scales on the meshing line.

Fig. 19 Bifurcation diagram of the low-speed gear pair

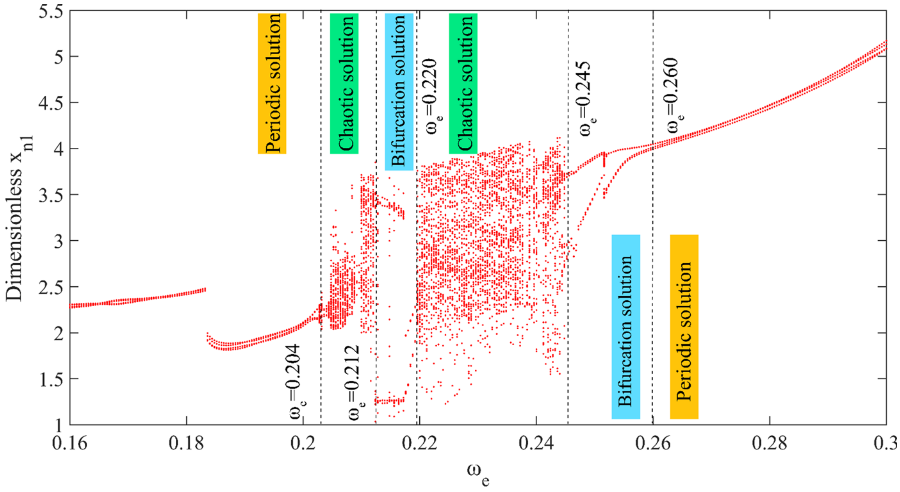

Fig. 20 Bifurcation diagram of the intermediate gear pair

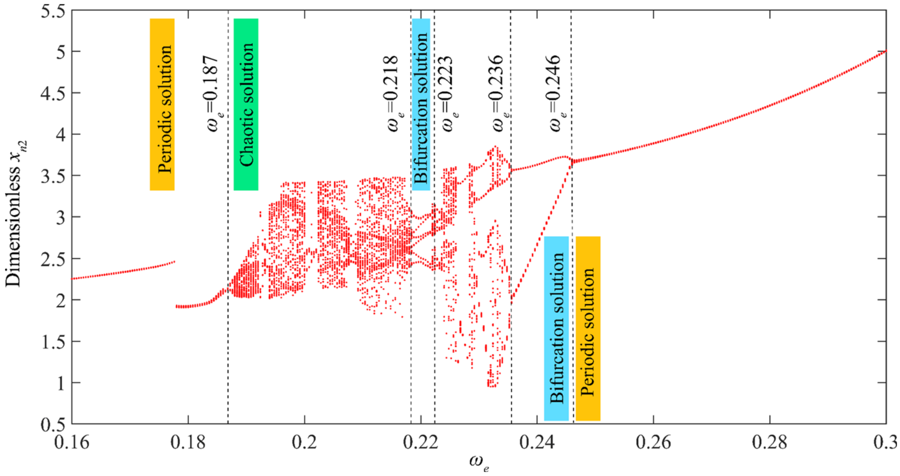

Fig. 21 Bifurcation diagram of the high-speed gear pair

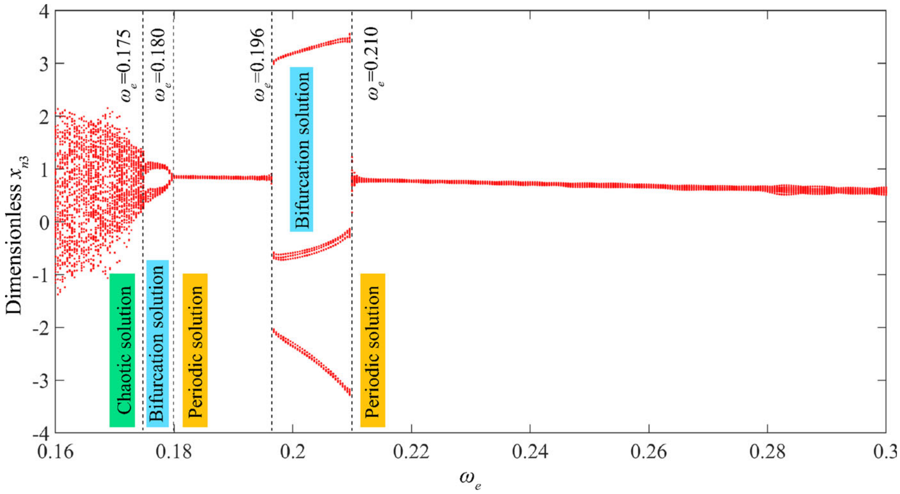

$$\bar{x}_n(\tau,\varepsilon)=\sum_{i=1}^{m}\varepsilon^i x_i(T_0,T_1,T_2,\ldots,T_m) \tag{68}$$

where m is the highest degree of higher order small quantity, and the value of m is determined by the calculation's need for precision. Time variables on various scales. It is possible to think of T_n as a function of m time variables and consider their independent variables.

Define the partial derivative operator $D_n=\partial/\partial T_n$ as shown in Eq. (69).

$$\begin{cases}\dfrac{\mathrm{d}}{\mathrm{d}\tau}=\sum\limits_{n=1}^{m}\varepsilon^n\dfrac{\partial}{\partial T_n}=D_0+\varepsilon D_1+\varepsilon^2 D_2+\cdots+\varepsilon^m D_m+\cdots\\ \dfrac{\mathrm{d}^2}{\mathrm{d}\tau^2}=\dfrac{\mathrm{d}}{\mathrm{d}\tau}\left(\sum\limits_{n=1}^{m}\varepsilon^n\dfrac{\partial}{\partial T_n}\right)=D_0^2+2\varepsilon D_0D_1+\varepsilon^2(D_1^2+2D_0D_1)+\cdots\end{cases} \tag{69}$$

Define the meshing frequency of gear teeth as $\omega=\omega_0+\varepsilon\omega_1+\varepsilon^2\omega_2+\ldots$, where ω_0 denotes the natural frequency of the intermediate gear pair. The meshing damping, meshing stiffness fluctuation term, and nonlinear term are defined as the same order quantities in order to produce an efficient approximation. $\zeta_{mi}=\varepsilon\zeta_{mi}, k=\varepsilon k, g_d=\varepsilon g_d, g_v=\varepsilon g_v, \delta_0=\varepsilon\delta_0$. Substituting the approximate solution $\bar{x}_n(\tau,\varepsilon)$ and partial derivative operator into Eqs. (70)–(72), only taking the first power of ε after expansion, and we may get the approximation differential equations for each order by equating the coefficients of the same power term of ε.

Take the differential equation of the intermediate gear pair as an example:

$$\begin{cases}\varepsilon^0: D_0^2x_0+\omega_0^2x_0=f_0+f\cos(v_2\tau)\\ \varepsilon^1: D_1^2x_1+\omega_1^2x_1=-2D_0D_1x_0\\ \qquad -(2\zeta_{m2}D_0D_1x_0-\delta_2x_0^3)\cos\alpha_n^{\mathrm{II}}\cos\beta^{\mathrm{II}}\\ \qquad -\omega_0^2k\cos(\omega_m\tau)x_0+g_dx_{0d}+g_vD_0x_{0v}\end{cases} \tag{70}$$

Suppose the solution of Eq. (71) is:

$$x_0=Ae^{i\omega_0T_0}+f_0/2\omega_0^2+\Lambda e^{iv_2T_0}+cc \tag{71}$$

where A represents the amplitude, $\Lambda=f/[2(\omega_0^2-v_2^2)]$, cc represents the conjugate complex number of the previous term, and v_2 is excitation the frequency of the external load.

Substituting Eq. (71) into Eq. (70), we obtain:

$$\begin{aligned}D_1^2x_1+\omega_0^2x_1=&-\left[2i\omega_0(D_1A+\zeta_{m2}A)+6\delta_2\cos\alpha_n^{\mathrm{II}}\cos\beta^{\mathrm{II}}A\Lambda^2\right.\\&\left.+3\delta_2\cos\alpha_n^{\mathrm{II}}\cos\beta^{\mathrm{II}}A^2\Lambda\right]e^{i\omega_0T_0}-\delta_2\cos\alpha_n^{\mathrm{II}}\cos\beta^{\mathrm{II}}\left[A^3e^{3i\omega_0T_0}+\Lambda^3e^{3iv_2T_0}\right.\\&+3A^2\Lambda e^{2i\omega_0T_0}e^{iv_2T_0}+3\bar{A}^2\Lambda e^{-2i\omega_0T_0}e^{iv_2T_0}+3A\Lambda^2e^{i\omega_0T_0}e^{2iv_2T_0}\\&+3A\Lambda^2e^{i\omega_0T_0}e^{-2iv_2T_0}+\frac{1}{2}\left(\frac{f_0}{2\omega_0^2}\right)^3+3{\frac{f_0}{\omega_0^4}}^{2}Ae^{i\omega_0T_0}+3{\frac{f_0}{\omega_0^4}}^{2}\Lambda e^{iv_2T_0}\\&+3\frac{f_0}{\omega_0^2}A^2e^{2iw_0T_0}+3\frac{f_0}{\omega_0^2}\Lambda^2e^{2iv_2T_0}+3A\bar{A}\frac{f_0}{\omega_0^2}+3\Lambda^2\frac{f_0}{\omega_0^2}\\&\left.+3\frac{f_0}{\omega_0^2}A\Lambda e^{i\omega_0T_0}e^{-iv_2T_0}+3\frac{f_0}{\omega_0^2}A\Lambda e^{i\omega_0T_0}e^{iv_2T_0}\right]\\&-\Lambda\left(2i\zeta_{m2}v_2+3\delta_2\cos\alpha_n^{\mathrm{II}}\cos\beta^{\mathrm{II}}\Lambda^2+6\cos\alpha_n^{\mathrm{II}}\cos\beta^{\mathrm{II}}A\bar{A}\right)e^{iv_2T_0}\\&-\frac{1}{2}k\omega_0^2\left(Ae^{i\omega_0T_0}+\frac{f_0}{\omega_0^2}+\Lambda e^{iv_2T_0}+\bar{A}e^{-i\omega_0T_0}+\Lambda e^{-iv_2T_0}\right)\cos\omega\tau\cos\alpha_n^{\mathrm{II}}\cos\beta^{\mathrm{II}}\\&+g_d\left[Ae^{i\omega_0(\tau-\tau_d)}+\frac{f_0}{\omega_0^2}+\Lambda e^{iv_2(\tau-\tau_d)}+\bar{A}e^{-i\omega_0(\tau-\tau_d)}+\Lambda e^{-iv_2(\tau-\tau_d)}\right]\\&+g_v\left[i\omega_0Ae^{i\omega_0(\tau-\tau_d)}+iv_2\Lambda e^{iv_2(\tau-\tau_d)}-i\omega_0\bar{A}e^{-i\omega_0(\tau-\tau_d)}\right.\\&\left.-iv_2\Lambda e^{-iv_2(\tau-\tau_d)}\right]+cc\end{aligned} \tag{72}$$

Because the superharmonic resonance of the system is examined in this part, the offset parameter of excitation frequency σ is added, making $3v_2=\omega_0+\varepsilon\sigma$. Equation (71) cosine function with excitation frequency is recast as follows in light of Eq. (67) and Euler equation:

$$\begin{aligned}\cos v_2\tau&=\cos\left(\frac{\omega_0+\varepsilon\sigma}{3}\tau\right)=\cos\left(\frac{\omega_0T_0+\sigma T_1}{3}\right)\\&=\frac{1}{2}e^{\frac{i\sigma T_1}{3}}e^{\frac{i\omega_0T_0}{3}}+cc\end{aligned} \tag{73}$$

Incorporate Eq. (73) into Eq. (72), and the following equation must be guaranteed in order to avoid the secular term.

$$\begin{aligned}&2i\omega_0D_1A+\delta_2\cos\alpha_n^{\mathrm{II}}\cos\beta^{\mathrm{II}}\\&\left(2i\omega_0\zeta_{m2}A+6A\Lambda^2+3A^2\bar{A}+3\Lambda^3e^{i\sigma T_1}+3\frac{f_0^2}{\omega_0^4}A\right)\\&+A\left(g_de^{-\omega_0\tau_d}-iw_0g_ve^{-i\omega_0\tau_v}\right)=0\end{aligned} \tag{74}$$

Rewrite A in Eq. (71) as: $A(T_1)=0.5\alpha(T_1)e^{i\beta(T_1)}$, where $A(T1)$ and $\beta(T1)$ stand for the slow variations in frequency and amplitude. By dividing the real and imaginary parts, the following equations can be produced.

$$\begin{cases}D_1\alpha=-\zeta_m\alpha\cos\alpha_n\cos\beta^{\mathrm{II}}+\dfrac{g_v\alpha\omega_0\cos\omega_0\tau_v}{2\omega_0}-\dfrac{g_d\alpha\sin\omega_0\tau_d}{2\omega_0}-\dfrac{\delta_2\cos\alpha_n\cos\beta^{\mathrm{II}}}{\omega_0}\Lambda^3\sin\varphi\\ \alpha D_1\varphi=\alpha\sigma+\dfrac{g_d\alpha\cos\omega_0\tau_d-g_v\alpha\omega_0\sin\omega_0\tau_d}{2\omega_0}-\dfrac{\delta_2\cos\alpha_n\cos\beta^{\mathrm{II}}}{\omega_0}\Lambda^3\cos\varphi\\ -\dfrac{24\alpha\Lambda^2\delta_2\cos\alpha_n\cos\beta^{\mathrm{II}}+3\alpha^3\delta_2\cos\alpha_n\cos\beta^{\mathrm{II}}+12\frac{f_0^2}{\omega_0^4}\alpha\delta_2\cos\alpha_n\cos\beta^{\mathrm{II}}}{8\omega_0}\end{cases} \tag{75}$$

where $\varphi = \sigma T_1 - \beta^{\mathrm{II}}$ describes the real-time phase of the intermediate gear pair.

The specific solution of Eq. (75) that matches the nonzero requirement corresponds to the system's steady periodic motion. If the algebraic equation that amplitude α and phase σ satisfy may be written as:

$$(\alpha\zeta_{m2}\cos\alpha_n\cos\beta^{\mathrm{II}} - W_1)^2 + (\alpha\sigma - W_2)^2 = W_3^2 \tag{76}$$

where W_1, W_2, W_3 can be expressed as:

$$\begin{cases} W_1 = \dfrac{g_v\alpha\omega_0\cos\omega_0\tau_v - g_d\alpha\sin\omega_0\tau_d}{2\omega_0} \\ W_2 = \dfrac{g_d\alpha\cos\omega_0\tau_d - g_v\alpha\omega_0\sin\omega_0\tau_v}{2\omega_0} - \dfrac{24\alpha\Lambda^2\delta_2 + 3\alpha^3\delta_2 + 12\alpha\delta_2 f_0^2/\omega_0^4}{8\omega_0}\cos\alpha_n\cos\beta^{\mathrm{II}} \\ W_3 = \dfrac{\delta_2\cos\alpha_n\cos\beta^{\mathrm{II}}}{\omega_0}\Lambda^3 \end{cases} \tag{77}$$

The stability of superharmonic resonance of the intermediate gear pair is analyzed. The characteristic equation of the equilibrium point of the system is:

$$\det\begin{bmatrix} V_1 - \lambda & -\alpha V_2 \\ \dfrac{1}{\alpha}\left(V_2 - \dfrac{3\delta_2\alpha\cos\beta\cos\alpha_n}{4\omega_0}\right) & V_1 - \lambda \end{bmatrix} = 0 \tag{78}$$

In Eq. (78),

$$\begin{cases} V_1 = \dfrac{g_v\omega_0\cos\omega_0\tau_v - g_d\sin\omega_0\tau_d}{2\omega_0} - \zeta_{m2}\cos\alpha_n\cos\beta^{\mathrm{II}} \\ V_2 = \sigma - \dfrac{3\alpha^2\delta_2 + 24\Lambda^2\delta_2 + 12f_0^2\delta_2}{8\omega_0}\cos\alpha_n\cos\beta^{\mathrm{II}} \end{cases} \tag{79}$$

It can be determined that the need for the system to stay stable when $\zeta_{m2} > 0$ is.

$$V_1^2 + V_2\left(V_2 - \frac{3\delta_2\alpha^2\cos\alpha_n\cos\beta^{\mathrm{II}}}{4\omega_0}\right) > 0 \tag{80}$$

5.2 Numerical analysis of superharmonic resonance

This part explores the impacts of meshing damping and time delay parameters in order to research the NW planetary gear system's dynamic characteristics. Define the initial parameters of Eq. (63), $k = 0.3$, $\zeta_{m1} = 0.06$, $f_1 = 1.0$, f I $0 = 0.2$, $g_{d1} = 0.1$, $g_{v1} = 0.1$,$\tau_{\mathrm{d}} = T/9$, $\tau_{\mathrm{v}} = T/9$. Define the initial parameters of Eq. (64), $k = 0.4$, $\zeta_{m2} = 0.05$, $f_2 = 4.0$, f II $0 = 0.5$, $g_{d2} = -0.1$, $g_{v2} = -0.05$,$\tau_{\mathrm{d}} = \mathrm{T}/9$, $\tau_{\mathrm{v}} = \mathrm{T}/9$. Define the initial parameters of Eq. (65), $k = 0.4$, $\zeta_{m3} = 0.05$, $f_3 = 4.0$, f III $0 = 0.5$, $g_{d3} = 0.2$, $g_{v3} = 0.1$,$\tau_{\mathrm{d}} = \mathrm{T}/9$, $\tau_{\mathrm{v}} = \mathrm{T}/9$.

5.2.1 *Low-speed gear pair*

The initial parameters are taken into account by Eq. (63). The family of amplitude–frequency characteristic curves with ζ_{m1} as the parameter, which depicts the connection between the system's amplitude α_1 and excitation frequency ω_1, is depicted in Fig. 22a. The shaded circle in Fig. 22a depicts the system's unstable branches when ζ_{m1} ranges from 0.02 to 0.08. The amplitude α_1 of the low-speed gear pair's superharmonic resonance lowers with an increase in ζ_{m1}, and the unstable branch gradually contracts. The unstable branch vanishes when ζ_{m1} is set to 0.1, demonstrating that meshing damping can be appropriately increased to improve the low-speed gear pair stability.

The family of amplitude–frequency characteristic curves with ζ_{m1} as the parameter, illustrating the connection between the amplitude and the meshing damping, is depicted in Fig. 22b. The amplitude α_1 of the low-speed gear pair's superharmonic resonance decreases with an increase in ζ_{m1} when ω_1 takes a value between 0.1590 and 0.1594. The amplitude α_1 of the low-speed gear pair's superharmonic resonance progressively develops unstable multi-branches when ω_1 exhibits a discontinuity 0.1596 and 0.1598, indicating that the curve will appear to contain multiple values. The region where the amplitude α_1 exhibits a discontinuity when $\omega_1 = 0.1598$ is indicated by the shaded area in Fig. 22b. As ζ_{m1} increases, the amplitude α_1 is slowly lower, moving from point A4 to point A3. With further increases in ζ_{m1}, the amplitude α_1 jumps from point A3 to point A1. After point A1, a steady decline in α_1 is observed along the curve. When the process is reversed, the amplitude α_1 jumps from point A2 to point A4.

The family of amplitude–frequency characteristic curves with g_{d1} as the parameter, depicting the relationship between the amplitude α_1 and excitation frequency ω_1, is depicted in Fig. 23a. The shaded circle in Fig. 23a depicts the unstable branches of the low-speed gear pair when g_{d1} ranges from -0.4 to 0. The unstable branch vanishes when g_{d1} is set to 0.2 and 0.4, demonstrating that appropriate displacement

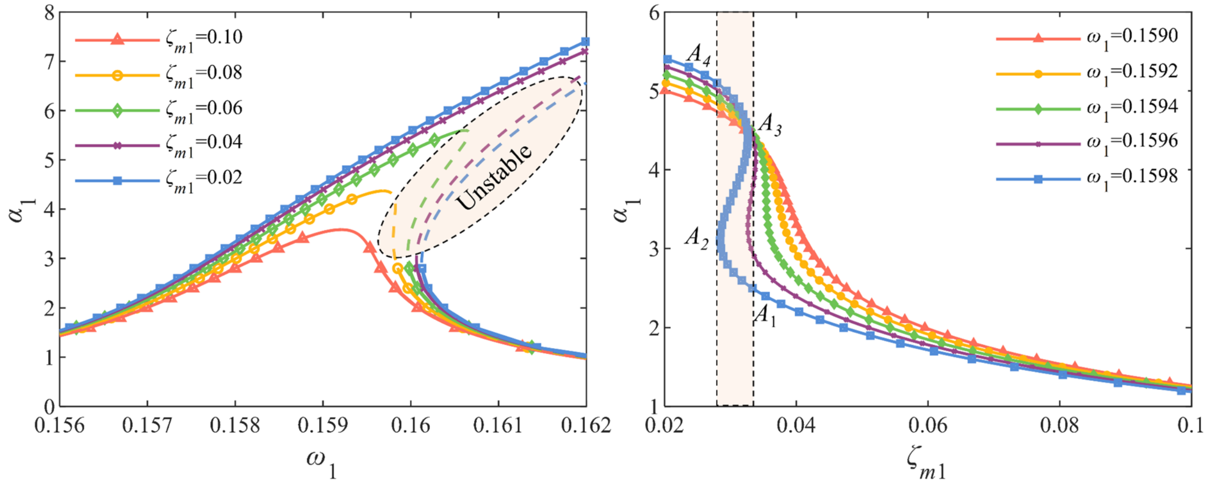

(a) Family of curves ω_1-α_1 (b) Family of curves ζ_{m1}-α_1

Fig. 22 Influence of meshing damping on the low-speed gear pair. **a** Family of curves ω_1-α_1, **b** Family of curves ζ_{m1}–α_1

control parameters can improve the low-speed gear pair stability.

The family of amplitude–frequency characteristic curves with g_{d1} as the parameter, illustrating the connection between the amplitude and the displacement control parameters, is depicted in Fig. 23b. The amplitude α_1 of the low-speed gear pair's superharmonic resonance drops with an increase in g_{d1} when ω_1 assumes 0.1590. The amplitude α_1 of the low-speed gear pair's superharmonic resonance progressively develops unstable multi-branch when g_{d1} takes 0.1592 to 0.1598, indicating that the curve will appear to contain multiple values. The region where the amplitude α_1 skips when ω_1 = 0.1598 is indicated by the shaded area in Fig. 23b. As g_{d1} increases, the amplitude α_1 is slowly lower, moving from point A4 to point A3, and as g_{d1} increases more, the amplitude α_1 skips from point A3 to point A1, after point A1, a steady decline in α_1 is seen along the curve. When the process is reversed, the amplitude α_1 skips from point A2 to point A4.

The family of amplitude–frequency characteristic curves with g_{v1} as the parameter, illustrating the connection between the amplitude α_1 and excitation frequency ω_1, is depicted in Fig. 24a. The shaded circle in Fig. 24a depicts the unstable branches when g_{v1} ranges from 0 to 0.4. The unstable branch vanishes when g_{v1} is set to − 0.2 and − 0.4, demonstrating that appropriate speed control parameters can improve the low-speed gear pair stability.

The family of amplitude–frequency characteristic curves with g_{v1} as the parameter, illustrating the connection between the amplitude and the speed control parameters, is depicted in Fig. 24b. The amplitude α_1 of the low-speed gear pair's superharmonic resonance increases rapidly with an increase in g_{v1} when ω_1 assumes 0.1590 and 0.1592. The amplitude α_1 of the low-speed gear pair's superharmonic resonance progressively develops unstable multi-branch when g_{v1} takes 0.1594 to 0.1598, indicating that the curve will appear to contain multiple values. The region where the amplitude α_1 skips when ω_1 = 0.1598 is indicated by the shaded area in Fig. 24b. As g_{v1} increases, the amplitude α_1 increases rapidly, moving from point A1to point A2, and as g_{v1} increases more, the amplitude α_1 skips from point A2 to point A4, after point A4, a steady decline in α_1 is seen along the curve. When the process is reversed, the amplitude α_1 skips from point A3 to point A1.

5.2.2 *Intermediate gear pair*

The initial parameters are taken into account by Eq. (64). The family of amplitude–frequency characteristic curves with ζ_{m2} as the parameter, which depicts the connection between the amplitude α_2 and excitation frequency ω_2, is depicted in Fig. 25a. The amplitude α_2 of the superharmonic resonance lowers with an increase in ζ_{m2}, and the unstable branch gradually contracts. The unstable branch vanishes when ζ_{m2} is set to 0.06, 0.08, and 0.10, demonstrating

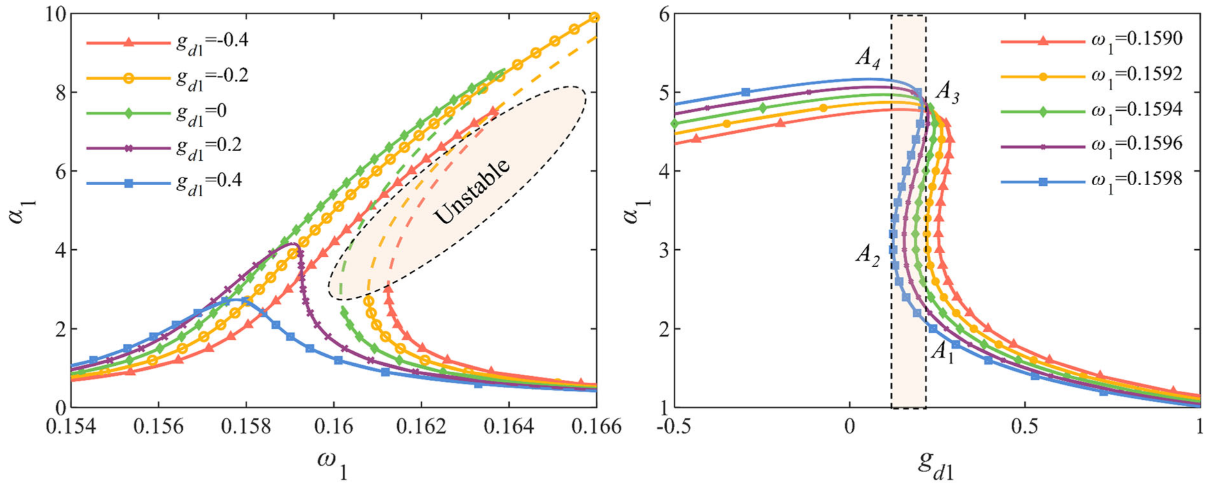

(a) Family of curves ω_1-α_1 (b) Family of curves g_{d1}-α_1

Fig. 23 Influence of displacement control parameters on the low-speed gear pair. **a** Family of curves ω_1–α_1, **b** Family of curves g_{d1}–α_1

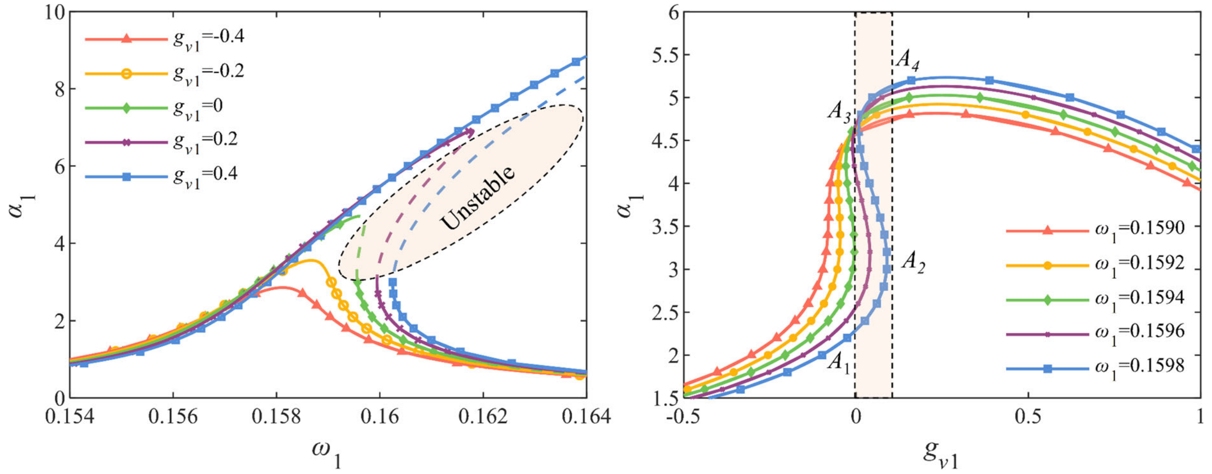

(a) Family of curves ω_1-α_1 (b) Family of curves g_{v1}-α_1

Fig. 24 Influence of speed control parameters on the low-speed gear pair. **a** Family of curves ω_1–α_1, **b** Family of curves g_{v1}–α_1

that meshing damping can be appropriately increased to improve the intermediate gear pair stability.

The family of amplitude–frequency characteristic curves with ζ_{m2} as the parameter, illustrating the connection between the amplitude and the meshing damping, is depicted in Fig. 25b. The amplitude α_2 of the superharmonic resonance drops with an increase in ζ_{m2} when ω_2 assumes a value between 0.3290 and 0.3296. The amplitude α_2 of the superharmonic resonance progressively develops unstable multi-branch when ω_2 takes 0.3298, indicating that the curve will appear to contain multiple values.

The family of amplitude–frequency characteristic curves with g_{d2} as the parameter, illustrating the connection between the amplitude α_2 and excitation frequency ω_2, is depicted in Fig. 26a. The unstable branch vanishes when g_{d2} is set to 0, 0.2, and 0.4, demonstrating that appropriate displacement control parameters can improve the stability.

The family of amplitude–frequency characteristic curves with g_{d2} as the parameter, which illustrates the connection between the amplitude and the displacement control parameters, is depicted in Fig. 26b. The amplitude α_2 of the superharmonic resonance drops

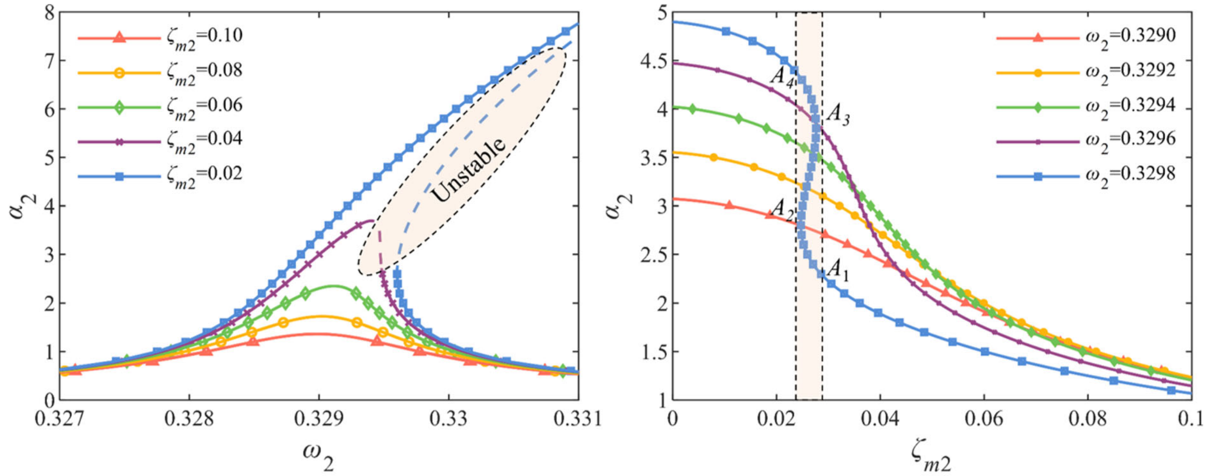

(a) Family of curves ω_2-α_2 (b) Family of curves ζ_{m2}-α_2

Fig. 25 Influence of meshing damping on the intermediate gear pair. **a** Family of curves ω_2–α_2, **b** Family of curves ζ_{m2}–α_2

with an increase in g_{d2} when ω_2 assumes 0.3294 to 0.3298. The amplitude α_2 of the superharmonic resonance progressively develops unstable multi-branch when g_{d2} takes 0.3300 to 0.3302, indicating that the curve will appear to contain multiple values.

The family of amplitude–frequency characteristic curves with g_{v2} as the parameter, illustrating the connection between the amplitude α_2 and excitation frequency ω_2, is depicted in Fig. 27a. The unstable branch vanishes when g_{v2} is set to 0, − 0.2, and − 0.4, demonstrating that appropriate speed control parameters can improve the stability.

The family of amplitude–frequency characteristic curves with g_{v2} as the parameter, which illustrates the connection between the amplitude and the speed control parameters, is depicted in Fig. 27b. The amplitude α_2 of the superharmonic resonance increases rapidly with an increase in g_{v2} when ω_2 assumes 0.3290 to 0.3294. The amplitude α_2 of the intermediate gear pair's superharmonic resonance progressively develops unstable multi-branch when g_{v2} takes 0.3296 and 0.3298, indicating that the curve will appear to contain multiple values.

5.2.3 *High-speed gear pair*

The initial parameters are taken into account by Eq. (65). The family of amplitude–frequency characteristic curves with ζ_{m3} as the parameter, which depicts the connection between the amplitude α_3 and excitation frequency ω_3, is depicted in Fig. 28a. The shaded circle in Fig. 28a depicts the high-speed gear pair's unstable branches when ζ_{m3} ranges from 0.02 to 0.04. The amplitude α_3 of the high-speed gear pair's superharmonic resonance lowers with an increase in ζ_{m3}, and the unstable branch gradually contracts. The unstable branch vanishes when ζ_{m3} is set to 0.06, 0.08, and 0.10, demonstrating that meshing damping can be appropriately increased to improve the high-speed gear pair stability.

The family of amplitude–frequency characteristic curves with ζ_{m3} as the parameter, illustrating the connection between the amplitude and the meshing damping, is depicted in Fig. 28b. The amplitude α_3 of the high-speed gear pair's superharmonic resonance drops with an increase in ζ_{m3} when ω_3 assumes a value between 0.3565 and 0.3568. The amplitude α_3 of the high-speed gear pair's superharmonic resonance progressively develops unstable multi-branch when ω_3 takes 0.3569, indicating that the curve will appear to contain multiple values. The region where the amplitude α_3 skips when ω_3 = 0.3569 is indicated by the shaded area in Fig. 28b.

The family of amplitude–frequency characteristic curves with g_{d3} as the parameter, illustrating the connection between the amplitude α_3 and excitation frequency ω_3, is depicted in Fig. 29a. The shaded circle in Fig. 29a depicts the high-speed gear pair's unstable branches when g_{d3} ranges from − 0.4 to 0. The unstable branch vanishes when g_{d3} is set to 0.2 and 0.4, demonstrating that appropriate displacement

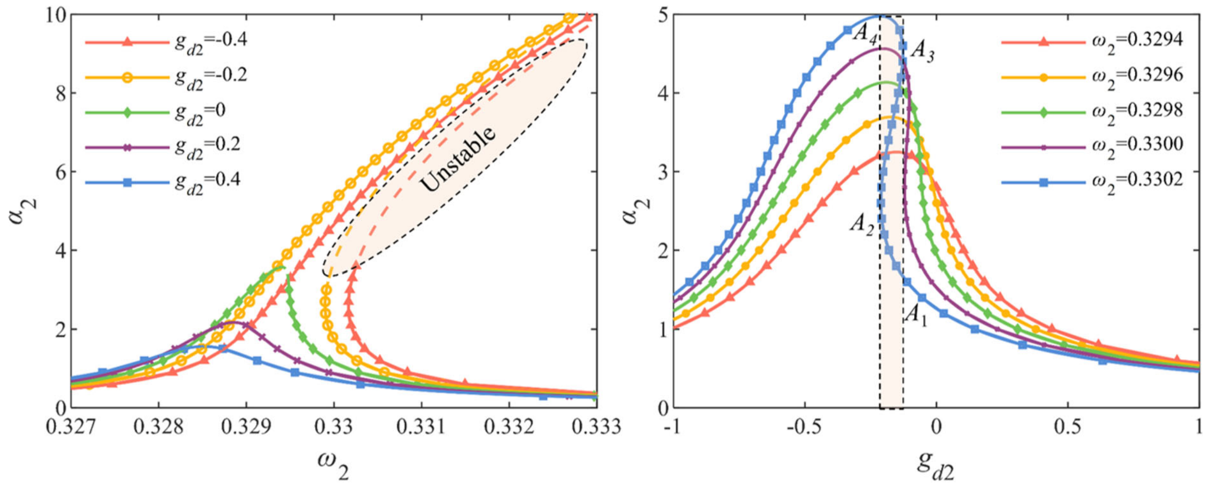

(a) Family of curves ω_2-α_2 (b) Family of curves g_{d2}-α_2

Fig. 26 Influence of displacement control parameters on the intermediate gear pair. **a** Family of curves ω_2–α_2, **b** Family of curves g_{d2}–α_2

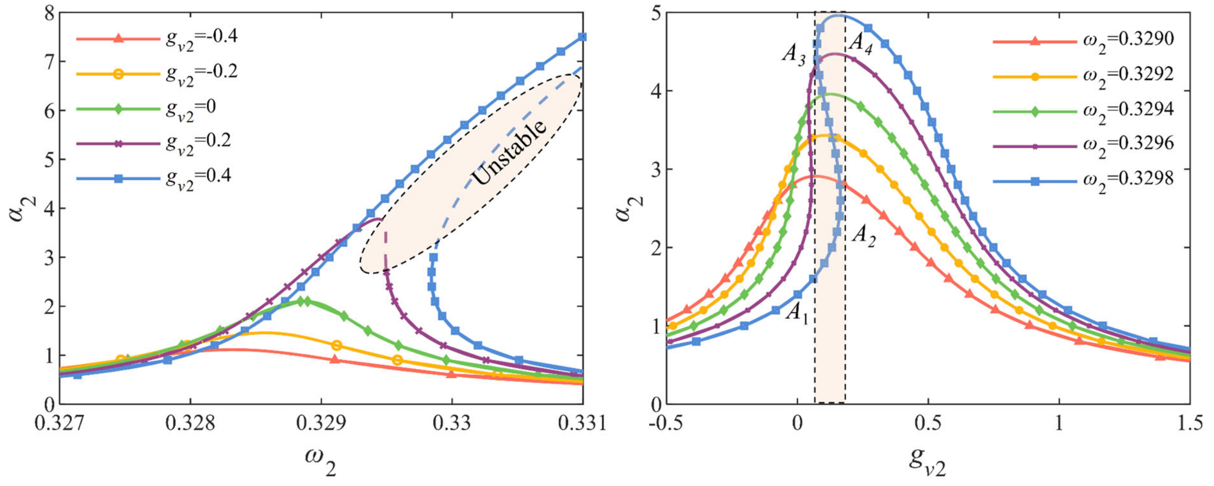

(a) Family of curves ω_2-α_2 (b) Family of curves g_{v2}-α_2

Fig. 27 Influence of speed control parameters on the intermediate gear pair. **a** Family of curves ω_2–α_2, **b** Family of curves g_{v2}–α_2

control parameters can improve the high-speed gear pair stability.

The family of amplitude–frequency characteristic curves with g_{d3} as the parameter, illustrating the connection between the amplitude and the displacement control parameters, is depicted in Fig. 29b. The amplitude α_3 of the high-speed gear pair's superharmonic resonance drops with an increase in g_{d3} when ω_3 assumes 0.3571 to 0.3577. The amplitude α_3 of the high-speed gear pair's superharmonic resonance progressively develops unstable multi-branch when g_{d3} takes 0.3579, indicating that the curve will appear to contain multiple values. The region where the amplitude α_3 skips when $\omega_3 = 0.3579$ is indicated by the shaded area in Fig. 29b.

The family of amplitude–frequency characteristic curves with g_{v3} as the parameter, illustrating the connection between the amplitude α_3 and excitation frequency ω_3, is depicted in Fig. 30a. The shaded circle in Fig. 30a depicts the high-speed gear pair's unstable branches when g_{v3} ranges from 0 to 0.4. The unstable branch vanishes when g_{v3} is set to − 0.2 and

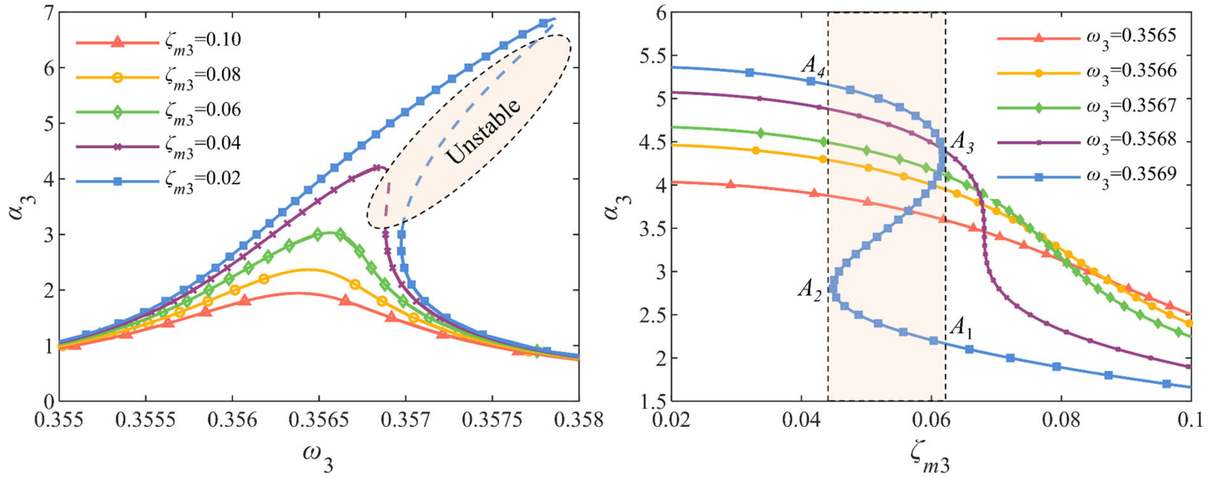

(a) Family of curves ω_3-α_3 (b) Family of curves ζ_{m3}-α_3

Fig. 28 Influence of meshing damping on the high-speed gear pair. **a** Family of curves ω_3–α_3, **b** Family of curves ζ_{m3}–α_3

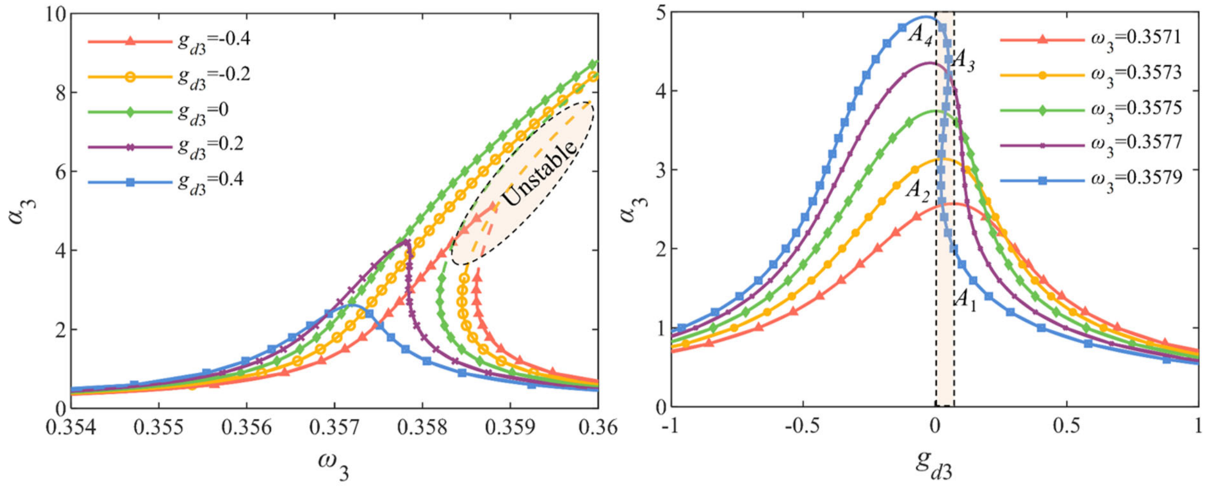

(a) Family of curves ω_3-α_3 (b) Family of curves g_{d3}-α_3

Fig. 29 Influence of displacement control parameters on the high-speed gear pair. **a** Family of curves ω_3–α_3, **b** Family of curves g_{d3}–α_3

− 0.4, demonstrating that appropriate speed control parameters can demonstrate that meshing damping can be appropriately increased to improve the high-speed gear pair stability.

The family of amplitude–frequency characteristic curves with g_{v3} as the parameter, illustrating the connection between the amplitude and the speed control parameters, is depicted in Fig. 30b. The amplitude α_3 of the high-speed gear pair's superharmonic resonance increases rapidly with an increase in g_{v3} when ω_3 assumes 0.3567 and 0.3568. The amplitude α_3 of the high-speed gear pair's superharmonic resonance progressively develops unstable multi-branch when g_{v3} takes 0.3569 to 0.3571, indicating that the curve will appear to contain multiple values. The region where the amplitude α_3 skips when $\omega_3 = 0.3571$ is indicated by the shaded area in Fig. 30b.

6 Conclusion

The method proposed in this paper considers the degree of freedom in four directions. Compared with

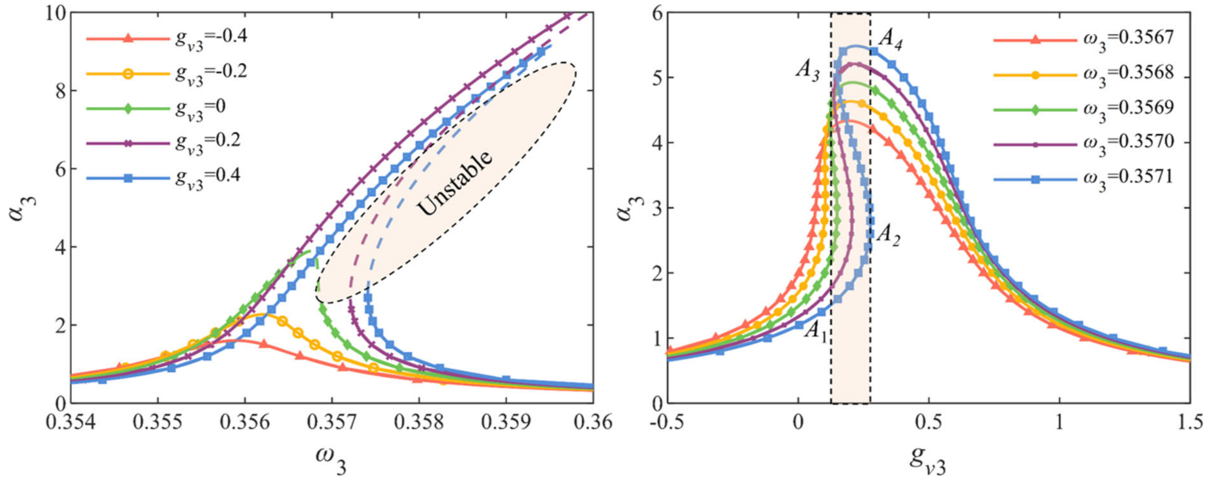

(a) Family of curves ω_3-α_3

(b) Family of curves g_{v3}-α_3

Fig. 30 Influence of speed control parameters on the high-speed gear pair. **a** Family of curves ω_3–α_3, **b** Family of curves g_{v3}–α_3

the pure torsional vibration model, the results of this paper have higher accuracy. In addition to the degree of freedom, this paper establishes a nonlinear dynamic model of wind power transmission system under multi-parameter coupling. Other studies do not consider the effects of random wind speed, bearing clearance and gear ring flexibility at the same time, which also shows that the research method proposed in this paper has higher accuracy. The main conclusions of this paper can be summarized as follows:

(1) The NW planetary gear-bearing system with bending-torsion coupling has rich nonlinear characteristics. With the change of parameter, NW planetary gear-bearing system will undergo periodic motion, bifurcation solution motion, and chaotic motion.

(2) Increasing meshing damping has obvious advantages in reducing unstable branches, preventing amplitude jumps, and suppressing excessive amplitude. Adjusting the displacement control parameters and speed control parameters is beneficial to reduce the system amplitude and improve the stability of the system.

(3) Due to the influence of stimulation frequency, the system will become unstable. In order to ensure the stability of the NW planetary gear-bearing system in the near-superharmonic resonance state, the excitation frequency needs to be adjusted.

Acknowledgements This research is financially supported by National Natural Science Foundation of China (No.52265004), Guangxi Science and Technology Major Program (No. AA23073019), Open Research Fund of State Key Laboratory of Precision Manufacturing for Extreme Service Performance, Central South University (No.Kfkt2023-06), Open Fund of State Key Laboratory of Digital Manufacturing Equipment and Technology, Huazhong University of Science and Technology (No. DMETKF2021017), National Key Laboratory of Science and Technology on Helicopter Transmission (No. HTL-0-21G07), and entrepreneurship and Innovation Talent Program of Taizhou City, Jiangsu Province.

Data availability The datasets generated during and/or analyzed during the current study are available from the corresponding author on reasonable request.

Declaration

Conflict of interest Authors declare that they have no conflicts with other people or organizations that can inappropriately influence our work.

References

1. Xin, G., Hamzaoui, N., Antoni, J.: Extraction of second-order cyclostationary sources by matching instantaneous power spectrum with stochastic model-application to wind turbine gearbox. Renewable Energy **147**, 1739–1758 (2020). https://doi.org/10.1016/j.renene.2019.09.087
2. Sequeira, C., Pacheco, A., Galego, P., Gorbeña, E.: Analysis of the efficiency of wind turbine gearboxes using the temperature variable. Renewable Energy **135**, 465–472 (2019). https://doi.org/10.1016/j.renene.2018.12.040
3. Shi, J., Gou, X., Zhu, L.: Generation mechanism and evolution of five-state meshing behavior of a spur gear system considering gear-tooth time-varying contact characteristics. Nonlinear Dyn. **106**(3), 2035–2060 (2021). https://doi.org/10.1007/s11071-021-06891-5

4. Cao, Z., Chen, Z., Jiang, H.: Nonlinear dynamics of a spur gear pair with force-dependent mesh stiffness. Nonlinear Dyn. **99**(2), 1227–1241 (2020). https://doi.org/10.1007/s11071-019-05348-0
5. Xiang, L., Gao, N.: Coupled torsion-bending dynamic analysis of gear-rotor-bearing system with eccentricity fluctuation. Appl. Math. Model. **50**, 569–584 (2017). https://doi.org/10.1016/j.apm.2017.06.026
6. Liu, P., Zhu, L., Gou, X., Shi, J., Jin, G.: Modeling and analyzing of nonlinear dynamics for spur gear pair with pitch deviation under multi-state meshing. Mech. Mach. Theory **163**, 104378 (2021). https://doi.org/10.1016/j.mechmachtheory
7. Wang, S., Zhu, R.: Nonlinear dynamic analysis of GTF gearbox under friction excitation with vibration characteristics recognition and control in frequency domain. Mech. Syst. Signal Process. **151**, 107373 (2021). https://doi.org/10.1016/j.ymssp.2020.107373
8. Wang, S., Zhu, R.: Theoretical investigation of the improved nonlinear dynamic model for star gearing system in GTF gearbox based on dynamic meshing parameters. Mech. Mach. Theory **156**, 104108 (2021). https://doi.org/10.1016/j.mechmachtheory.2020.104108
9. Wang, S., Zhu, R.: Study on load sharing behavior of coupling gear-rotor-bearing system of GTF aero-engine based on multi-support of rotors. Mech. Mach. Theory **147**, 103764 (2020). https://doi.org/10.1016/j.mechmachtheory
10. Hu, B., Zhou, C., Wang, H., Chen, S.: Nonlinear tribo-dynamic model and experimental verification of a spur gear drive under loss-of-lubrication condition. Mech. Syst. Signal Process. **153**, 107509 (2021). https://doi.org/10.1016/j.ymssp.2020.107509
11. Zhang, X., Zhong, J., Li, W., Bocian, M.: Nonlinear dynamic analysis of high-speed gear pair with wear fault and tooth contact temperature for a wind turbine gearbox. Mech. Mach. Theory **173**, 104840 (2022). https://doi.org/10.1016/j.mechmachtheory.2022.104840
12. Chang-Jian, C.W.: Nonlinear analysis for gear pair system supported by long journal bearings under nonlinear suspension. Mech. Mach. Theory **45**(4), 569–583 (2010). https://doi.org/10.1016/j.mechmachtheory.2009.11.001
13. Li, Z.F., Zhu, L.Y., Chen, S.Q., Chen, Z.G., Gou, X.F.: Study on safety characteristics of the spur gear pair considering time-varying backlash in the established multilevel safety domains. Nonlinear Dyn. **109**, 1297–1324 (2022). https://doi.org/10.1007/s11071-022-07467-7
14. Mo, S., Li, Y., Luo, B., Wang, L., Bao, H., Cen, G., Huang, Y.: Research on the meshing characteristics of asymmetric gears considering the tooth profile deviation. Mech. Mach. Theory **175**, 104926 (2022). https://doi.org/10.1016/j.mechmachtheory.2022.104926
15. Mo, S., Song, Y., Feng, Z., Song, W., Hou, M.: Research on dynamic load sharing characteristics of double input face gear split-parallel transmission system. Proc. Inst. Mech. Eng. C J. Mech. Eng. Sci. **236**(5), 2185–2202 (2022). https://doi.org/10.1177/09544062211026349
16. Mo, S., Zhang, Y., Luo, B., Bao, H., Cen, G., Huang, Y.: The global behavior evolution of non-orthogonal face gear-bearing transmission system. Mech. Mach. Theory **175**, 104969 (2022). https://doi.org/10.1016/j.mechmachtheory
17. Shuai, M., Yingxin, Z., Yuling, S., Wenhao, S., Yunsheng, S.: Nonlinear vibration and primary resonance analysis of non-orthogonal face gear-rotor-bearing system. Nonlinear Dyn. **108**, 3367–3389 (2022). https://doi.org/10.1007/s11071-022-07432-4
18. Shuai, M., Ting, Z., Guo-Guang, J., Xiao-lin, C., Han-jun, G.: Analytical investigation on load sharing characteristics of herringbone planetary gear train with flexible support and floating sun gear. Mech. Mach. Theory **144**, 103670 (2020). https://doi.org/10.1016/j.mechmachtheory.2019.103670
19. Zhao, Y., Ahmat, M., Bari, K.: Nonlinear dynamics modeling and analysis of transmission error of wind turbine planetary gear system proceedings of the institution of mechanical engineers, Part K. J. Multi-body Dyn. **228**(4), 438–448 (2014). https://doi.org/10.1177/1464419314536888
20. Li, S., Wu, Q., Zhang, Z.: Bifurcation and chaos analysis of multistage planetary gear train. Nonlinear Dyn. **75**(1), 217–233 (2014). https://doi.org/10.1007/s11071-013-1060-z
21. Wei, J., Zhang, A., Qin, D., Lim, T., Shu, R., Lin, X., Meng, F.: A coupling dynamics analysis method for a multistage planetary gear system. Mech. Mach. Theory **110**, 27–49 (2017). https://doi.org/10.1016/j.mechmachtheory.2016.12.007
22. Xiang, L., Gao, N., Hu, A.: Dynamic analysis of a planetary gear system with multiple nonlinear parameters. J. Comput. Appl. Math. **327**, 325–340 (2018). https://doi.org/10.1016/j.cam.2017.06.021
23. Qiu, X., Han, Q., Chu, F.: Load-sharing characteristics of planetary gear transmission in horizontal axis wind turbines. Mech. Mach. Theory **92**, 391–406 (2015). https://doi.org/10.1016/j.mechmachtheory.2015.06.004
24. Zhao, M., Ji, J.C.: Nonlinear torsional vibrations of a wind turbine gearbox. Appl. Math. Model. **39**(16), 4928–4950 (2015). https://doi.org/10.1016/j.apm.2015.03.026
25. Chen, H., Wang, X., Gao, H., Yan, F.: Dynamic characteristics of wind turbine gear transmission system with random wind and the effect of random backlash on system stability, proceedings of the institution of mechanical engineers Part C. J. Mech. Eng. Sci. **231**(14), 2590–2597 (2017). https://doi.org/10.1177/0954406216640572
26. Guo, Y., Keller, J., Parker, R.G.: Nonlinear dynamics and stability of wind turbine planetary gear sets under gravity effects. Eur. J. Mech. A. Solids **47**, 45–57 (2014). https://doi.org/10.1016/j.euromechsol.2014.02.013
27. Zhu, C., Xu, X., Liu, H., Luo, T., Zhai, H.: Research on dynamical characteristics of wind turbine gearboxes with flexible pins. Renewable Energy **68**, 724–732 (2014). https://doi.org/10.1016/j.renene.2014.02.047
28. Zhang, Q., Wang, X., Wu, S., Cheng, S., Xie, F.: Nonlinear characteristics of a multi-degree-of-freedom wind turbine's gear transmission system involving friction. Nonlinear Dyn. **107**(4), 3313–3338 (2022). https://doi.org/10.1007/s11071-021-07092-w
29. Moradi, H., Salarieh, H.: Analysis of nonlinear oscillations in spur gear pairs with approximated modelling of backlash nonlinearity. Mech. Mach. Theory **51**, 14–31 (2012). https://doi.org/10.1016/j.mechmachtheory.2011.12.005
30. Wang, J., Lv, B., Sun, R., Zhao, Y.: Resonance and stability analysis of a cracked gear system for railway locomotive.

Appl. Math. Model. **77**, 253–266 (2020). https://doi.org/10.1016/j.apm.2019.07.039

31. Li, C.J., Lee, H., Choi, S.H.: Estimating size of gear tooth root crack using embedded modelling. Mech. Syst. Signal Process. **16**(5), 841–852 (2002). https://doi.org/10.1006/mssp.2001.1452